


Self-excited instability regimes of a confined turbulent jet flame at elevated pressure

Cite as: Phys. Fluids **34**, 044103 (2022); <https://doi.org/10.1063/5.0083293>

Submitted: 23 December 2021 • Accepted: 10 March 2022 • Published Online: 04 April 2022

 Timo Buschhagen,  Rohan M. Gejji,  Carlo Scalo, et al.

COLLECTIONS

 This paper was selected as Featured



View Online



Export Citation



CrossMark

APL Machine Learning

Open, quality research for the networking communities

OPEN FOR SUBMISSIONS MAY 2022

LEARN MORE



Self-excited instability regimes of a confined turbulent jet flame at elevated pressure

Cite as: Phys. Fluids **34**, 044103 (2022); doi: [10.1063/5.0083293](https://doi.org/10.1063/5.0083293)

Submitted: 23 December 2021 · Accepted: 10 March 2022 ·

Published Online: 4 April 2022



View Online



Export Citation



CrossMark

Timo Buschhagen,¹  Rohan M. Gejji,^{1,a)}  Carlo Scalo,²  and Carson D. Slabaugh¹ 

AFFILIATIONS

¹School of Aeronautics and Astronautics, Purdue University, West Lafayette, Indiana 47907, USA

²School of Mechanical Engineering, Purdue University, West Lafayette, Indiana 47907, USA

^{a)}Author to whom correspondence should be addressed: rgejji@purdue.edu

ABSTRACT

The dynamic response of a confined, premixed turbulent jet flame is investigated at high thermal power densities (~ 25 MW/m²/bar) and turbulence levels ($Re_{jet} \sim 5 \times 10^5$). As equivalence ratio and inlet jet velocity are varied at these conditions, multiple instability modes coexist: a low-amplitude instability ($p'/p_C \lesssim 9\%$) with longitudinal-mode fluctuations (1L and 2L) and two high-amplitude ($p'/p_C \lesssim 20\%$), high-frequency, transverse instability modes. While the axial modes are ubiquitous across the operational envelope, the transverse mode selection is sensitive to the equivalence ratio and reactant jet velocity. A linear stability analysis (LSA) of the confined base flow is performed to explore the flame perturbation in response to the density and temperature gradients, and the shear-layer instabilities in the flow. The high-frequency combustion instabilities are associated with a combined azimuthal hydrodynamic mode of the reactant jet, (1) at the combustion chamber near field and, (2) downstream in the fully developed region of the combustor. An excellent agreement was observed between the convectively unstable modes identified by the temporal LSA and the self-excited combustion instabilities in the experiment.

Published under an exclusive license by AIP Publishing. <https://doi.org/10.1063/5.0083293>

I. INTRODUCTION

Combustion instabilities result from the resonant coupling of an unsteady combustion process with acoustic and hydrodynamic modes of the combustor and can result in detrimental high-amplitude pressure oscillations. Fundamental insight into these instabilities has been primarily gained through studies in low-power canonical atmospheric or moderate pressure combustors facilitating laboratory scale operation and detailed diagnostics.^{1–7} Complex chamber geometries, high flame-power densities, and elevated pressures found in actual engines, however, shift and broaden the spectrum of spatiotemporal scales of flame–flow interactions, increasing susceptibility to combustion instabilities in longitudinal, transverse, and azimuthal chamber mode frequencies.⁸ This fact motivates the pursuit of experimental characterization of combustion instabilities at realistic flow conditions.

Transverse instabilities in air-breathing combustors are often encountered in multi-injector configurations through flame interactions between neighboring injector elements. These have also been reproduced in single-injector configurations through external excitation using acoustic drivers or periodic forcing of the fuel supply.⁴ Such studies have aided both fundamental understanding of the problem as well as the development of predictive capabilities for combustion dynamics through detailed and low-order computational models.

Hardi *et al.*⁹ investigated transverse instabilities in a high-pressure liquid oxygen and gaseous hydrogen flame with external excitation and found that intrinsic hydrodynamic instability of the liquid oxygen jet in response to transverse acoustic forcing played a dominant role in the observed high-amplitude instabilities. Similar observations were made by Urbano *et al.*¹⁰ using large-eddy simulations of a multi-element combustor. A self-excited transverse mode instability in a single injector liquid oxygen/methane propelled rocket combustor was investigated by Sliphorst *et al.*,¹¹ where a spinning transverse mode was observed, with precession about the chamber centerline with a preferred orientation linked to combustor asymmetry. Hummel¹² and Berger¹³ characterized a traveling transverse mode in a swirl-stabilized atmospheric burner in which flame displacement and deformation of the reaction zone in response to the chamber acoustic field resulted in a sustained limit cycle instability. Self-excited transverse combustion instabilities in a jet-stabilized flame were investigated by Buschhagen *et al.*¹⁴ in a high-pressure natural gas fueled combustor. The presence of high-frequency dynamics was correlated with an asymmetric vortex shedding mode near the combustor dump plane. Longitudinal instability modes were dominant in the absence of this asymmetry. The study of high-frequency thermoacoustic combustion instabilities beyond these limited studies has been limited to atmospheric pressure

experiments, in transverse or annular multi-injector configurations, with or without external acoustic excitation.^{4,15–17}

Intrinsic hydrodynamic instabilities present in complex reacting flow fields provide a fundamental link between pressure and heat release perturbations, as velocity perturbations induce local fluctuations in energy release through flame surface modulations.^{18,19} As a majority of the heat release occurs in the shear layer that forms between the reactant jet potential core and the surrounding recirculation region, the flame is subject to the inherent instabilities of the confined jet flow. Eddies and subsequent larger coherent structures forming in the shear layer downstream of the sudden expansion modulate the transport of heat, mass, and momentum within the reaction zone and lead to fluctuations in the flame heat release. The interaction between these turbulent flame processes and the resonant acoustic field are often linked through hydrodynamic characteristics of the flow, resulting in closely coupled velocity, temperature, and density fields. Local pressure oscillations in turn influence the gas properties which closes the complex feedback loop leading to the natural propensity to unstable behavior of turbulent flames. An asymmetry in the flow field promotes spatial asymmetry in the distribution of local heat release, which has the potential to drive transverse combustion instabilities.^{5,20–26} At sufficiently high levels of turbulence and flame thermal power densities, the axial and transverse combustion instability modes can achieve high limit-cycle amplitudes as observed in the current experiment.

The effect of jet confinement, velocity, and density ratio between the inner and outer flows are essential toward the stability of planar and round jet/wake flows.^{27,28} Two instability modes in these type of flows are found, where the first mode is associated with the instability of the shear layer itself, characterizing the roll-up process due to the velocity difference between the inner and outer fluid layers. The second mode is associated with the bulk motion of the jet/wake at larger axial wavelengths compared with the first mode, which leads to bulging, spiraling, or flapping of the jet/wake body. At intermediate confinement levels, the fundamental modes of bulk motion of the inner and outer flow interact and are seen to generate combined modes due to resonance if their wave numbers are compatible, generating a standing wave. These flows are particularly unstable, whereas flows with larger wave number separation in the inner and outer regions are generally more stable.

The externally forced hydrodynamic response of an axisymmetric jet located at velocity and pressure nodes of a standing mode was recently explored by Aesoy *et al.*²⁹ Axisymmetric and azimuthal modes were excited through changes in the jet exit boundary condition at the pressure and velocity antinodes, respectively. At intermediate locations, both modes were simultaneously driven as a result of asymmetric forcing of the transverse and longitudinal modes of the experiment. Axial disturbances at the nozzle exit typically evolve into axisymmetric jet modes, whereas azimuthal disturbances generate asymmetric modes. Mode switching is often observed when stochastic disturbances are present. Counter-rotating helical modes have identical stability properties, and if they are present at similar frequency and amplitudes result in a flapping instability through their superposition.^{11,15,30} Asymmetric modes disintegrate over much shorter streamwise distances than axisymmetric modes, transferring energy toward smaller turbulent length scales more efficiently. For these modes, the asymmetry in the velocity field results in periodic roll-up of two vortex

rings out of phase with each other. As these rings are convected with the mean combustor flow, they interact with each other resulting in rapid breakdown with higher jet spreading rate compared to axisymmetric modes.

Linear stability analysis (LSA) has been successfully applied to determine the spatiotemporal stability characteristics of complex flow fields in which a distinction is made between convectively (CU) and absolutely (AU) unstable flows. CU flows feature perturbations that grow downstream of an initial impulse in space and time, but decay at the spatial location of the initial impulse. By contrast, AU modes do not decay in time and have the potential to contaminate the whole flow field, if the absolutely unstable region is sufficiently large, yielding a global mode with a behavior comparable to a self-excited oscillator.^{31–33} Applied to combustion instability problems, LSA can help elucidate the nature of the underlying coupling mechanisms, where the concepts of convective and absolute flow instabilities are employed.^{34–36} Instability modes are assigned to acoustic eigenfrequencies of the combustor geometry, where amplification of the acoustic field through resonant coupling of the pressure and heat release rate fluctuations is observed. The existence of modes with frequencies that do not correspond to acoustic modes of the combustor geometry points to the presence of an CU global mode of the flow for which the flow field itself acts as a resonator. Both scenarios can be achieved by convective and absolute flow instabilities. AU modes are self-sustained hydrodynamic oscillations that in turn yield heat release fluctuations due to flow–flame interaction, which result in pressure oscillations at the characteristic frequency of the global mode, given that the acoustic field does not provide sufficient damping at that frequency. AU flows with characteristic frequencies similar to combustor acoustic eigenmodes generate high-amplitude limit-cycle behavior. CU flows readily amplify flow perturbations over a wide range of frequencies, though a preferred frequency exists for which the downstream amplification is maximum. If the preferred frequency is similar to natural acoustic resonance of the combustor, the flow-acoustic coupling sustains the convective instability, yielding synchronized heat release fluctuations that in turn provide energy to the acoustic field.

Ghoniem *et al.*³⁴ summarized evidence for the existence of AU global modes in shear layer stabilized premixed combustion systems. For a backward-facing step configuration similar to one described in the current study, a global mode was identified represented by vortex shedding and the subsequent pairing of these in the region of recirculating flow. High back-flow magnitudes paired with small shear layer thicknesses were found to support a CU to AU transition of the global mode. A similar study for backward-facing step combustors at atmospheric pressure was performed by Manoharan and Hemchandra³⁶ with consistent observations. A collocation of inflection points in the density and velocity profile was found to suppress an AU mode, and a positive or negative displacement was found to decrease or increase the growth rate of the most unstable mode. The baroclinic torque generated by different amplitudes of reaction shear layer displacement either amplified or dampened the Kelvin–Helmholtz instability at the shear layer where the flame was stabilized.

The predictive capability of LSA for instabilities in swirl-stabilized flames has also been demonstrated, primarily at atmospheric pressure.^{37,38} Oberleithner *et al.*³⁷ studied the influence of the flame shape on the existence or suppression of a precessing vortex core (PVC) located in the shear layer, separating the inner recirculation

zone from the annular swirling jet using LSA. Here, the density profile associated with the different flame shapes studied was found to determine whether the global flow field mode related to the presence of the PVC is AU or CU. Paredes *et al.*³⁸ compared the predictive capabilities of local and global LSA for swirl flames with a range of swirl numbers, including those that promoted the presence of a precessing vortex core. At low swirl numbers, where flow was primarily parallel to the mean flow, local LSA was sufficient, but at higher swirl numbers, global LSA was necessary to avoid overestimation of growth rate of unstable modes. The predictive capability of LSA to identify multiple unstable flow features in reacting flow fields for relatively low computational resources provides a promising route for understanding the sensitivity of operating parameters on the amplification of axial and transverse combustion instabilities in the current experiment.

This paper presents a combined experimental and theoretical investigation of combustion instabilities in a single-element turbulent jet flame operated at high pressure ($p_C \sim 7$ bar).^{14,39,40} The high power density conditions are fertile ground for a multitude of self-excited longitudinal and transverse, which are analyzed as a function of equivalence ratio, ϕ , inlet air temperature, T_{IN} , and inlet jet velocity, u_{IN} . An excellent match is observed between experiments and linear stability analysis (LSA), in spite of the extreme operating conditions. This work extends the conclusions from prior studies to high-power confined jet flames at elevated mean chamber pressure. The key contributions of the present study can be summarized in the following points:

- (i) Operating conditions of a single-element combustor have been pushed to high thermal power densities (~ 25 MW/m²/bar), flame confinement, and turbulence levels (reactant jet Reynolds number, $Re_{jet} \sim 5 \times 10^5$), triggering multiple self-sustaining axial and transverse instability modes, in the absence of external excitations or flame–flame interactions commonly found in multi-element combustors;
- (ii) Longitudinal modes are sustained across the entire equivalence ratio/inlet flow velocity (ϕ/u_{IN}) operational envelope of the combustor.
- (iii) Two distinct high-frequency modes are observed near the fundamental transverse mode of the combustion chamber, one at approximately 5 kHz (HF1) and the other at 6 kHz (HF2).
- (iv) Linear stability analysis (LSA) of the confined base flow confirmed the presence of two high-frequency hydrodynamic instability modes: HF1, corresponding to a combined azimuthal hydrodynamic mode of the jet at the combustion chamber near field; and HF2, observed in the wake of the jet flame, further downstream in the fully developed region of the combustor.

II. EXPERIMENTAL CONFIGURATION

A. Combustor hardware

The experiments were performed in a single-element model combustor operated at a mean chamber pressure of 7 bar with natural gas and heated air. Self-excited longitudinal and transverse combustion instabilities were observed across a range of equivalence ratios ($\phi = 0.6$ – 0.8) and air temperatures ($T_{IN} = 650$ – 800 K). A schematic of the combustion experiment is shown in Fig. 1. The flow path through the premixed duct (PD) and combustion chamber (CC) is

circular and axisymmetric throughout the length of the channel. The premixed duct (PD) is 720 mm in length and has a diameter of 40 mm. The combustion chamber is 1.2 m in length and has a diameter of 80 mm. A backward-facing step stabilizes the jet flame in the combustion chamber (CC), with an CC:PD expansion area ratio of four. Reactants are fully premixed with an external premixing device, then supplied to the PD through a choked orifice plate. The choked inlet condition isolates injection and mixing processes from pressure fluctuations downstream. It also provides a well-defined acoustic and flow boundary condition at the upstream end of the combustor. A sonic nozzle at the exit of the combustion chamber similarly provides a well-defined acoustic exit boundary condition and pressurizes the combustor. Reactant flows into the external premixer are controlled and metered with critical-flow venturi nozzles that conform to ASME and ISO specifications.^{41,42} The oxidizer used in this study was heated, dry air, and the fuel was pipeline natural gas with a composition of 92% CH₄, 6% C₂H₆, 0.5% CO₂, 0.3% C₃H₈, and 1.5% N₂. Ignition is achieved with a laser-induced spark, delivered when the reactant flows have stabilized at the target test conditions.

B. Combustor acoustics

The acoustic boundaries of the axial modes in the combustor are set by a choked orifice plate at the inlet of the premixed duct and the choked nozzle at the exit of the combustion chamber. The high expansion ratio between the combustion chamber and the premixed duct results in a high aspect ratio flame, with heat release concentrated in the shear layer of the reactant jet and surrounding recirculation zone. A simplified schematic is shown in Fig. 2, depicting the jet core at the reactant temperature T_{IN} and the surrounding volume of recirculated products at temperature T_C , which is approximated by the adiabatic flame temperature, T_{ad} . The jet-stabilized flame is considered to be acoustically compact for axial dynamics in the combustion chamber, as the mean flame length is relatively small compared to the longitudinal wavelengths of interest ($\lambda_{1L,system} = 1.92$ m). In the axial direction, the direction of acoustic wave propagation is parallel to the direction of mean flow. Conversely, transverse dynamics in the chamber are normal to the direction of mean flow and propagate through an inhomogeneous temperature field, especially in the region where the heat release from the flame is a significant fraction of the transverse acoustic wavelength. The flame is spatially non-compact with respect to the wavelength of transverse acoustic mode in the combustion chamber ($\lambda_{1T,CC} = 0.16$ m).

The longitudinal and transverse mode shapes for pressure, velocity, and density in the combustor are presented in Fig. 2, which were calculated using the axial and radial acoustic models detailed in Appendixes A–D. The inlet and exit boundaries of the combustion chamber are treated as acoustically closed boundaries, $u' = 0$ for simplicity. The p' and $m' = \rho Au'$ mode shapes for the fundamental longitudinal mode (1L) in the combustion chamber and its harmonic frequency (2L) are shown in Figs. 2(a) and 2(b). At the 1L frequency in the combustion chamber, a pressure anti-node and velocity node is present at the entrance to the combustion chamber. The 1L frequency varies from 360 to 385 Hz over the combustor operating range. As shown in Figs. 2(c)–2(g), the transverse frequency variation is much broader as the acoustic speed in the transverse direction is a function of both the operating condition and the flame shape. The dashed line in Fig. 2(c) corresponds to the expected 1T frequency for

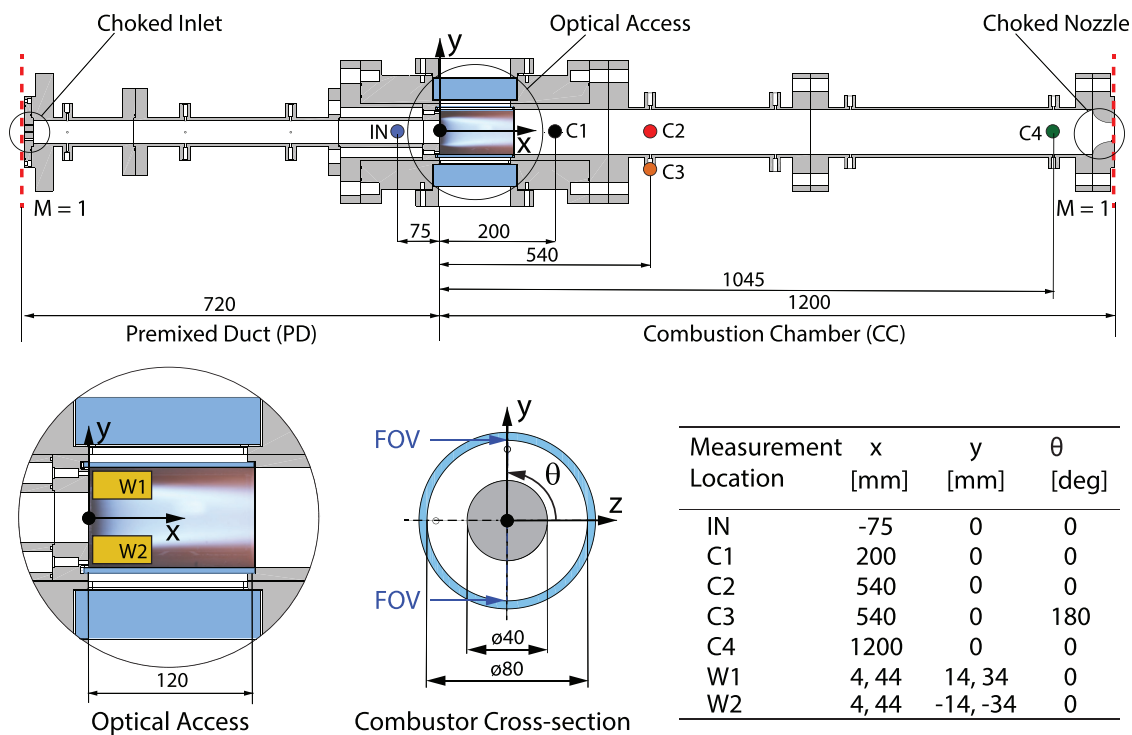


FIG. 1. Schematic of the combustor with instrumentation port locations. Pressure instrumentation locations IN, C1, C2, C3, and C4, and chemiluminescence probe locations W1 and W2 in the optical field of view (FOV) are reported in the table. All dimensions in mm.

homogeneous speed of sound in the combustion chamber cross section at T_{ad} . The span of estimated 1T frequency from 5 to 6.2 kHz agrees closely with the frequencies observed in the experiments, which will be discussed further in Secs. III–VI.

C. Instrumentation and diagnostics

Pressure fluctuations are measured at multiple locations throughout the system with water-cooled, high-frequency piezoresistive transducers (Kulite WCT312M), which have a natural resonance frequency of 1.65 MHz. The transducers are installed in recessed Helmholtz resonator cavities with a frequency >14 kHz and are sampled at 180 kHz. This installation reduces the thermal load on the sensor element with minimal impact to the accuracy of unsteady pressure measurements within the flow.^{43–45} The location of the pressure transducers on the combustion chamber is highlighted on the combustor schematic and denoted by the table in Fig. 1. Pressure measurements at locations IN, C1, C2, and C4 are aligned along the same azimuthal angle $\theta = 0^\circ$, whereas C3 is located diametrically opposite ($\theta = 180^\circ$) to C2 at the same axial position. A single pressure measurement was also located in the external premixer to verify isolation of the premixing system from dynamics within the combustion experiment.

The flame is imaged through a 120-mm cylindrical optical access at the upstream end of the CC. Chemiluminescence emission from electronically excited hydroxyl radicals (OH^*) was recorded at 50 kHz in the optical section of the combustion chamber. A UV filter, centered at 320 nm with 40 nm bandwidth (Semrock 320/40 Brightline Bandpass), was used to isolate the signal from background luminosity.

The light was collected by a 98 mm focal-length, $f/2.8$ objective lens (Cerro Soder Type-2178), then amplified by a Lambert HiCAT 25 intensifier with 1:1 relay lens and recorded with a Phantom v2512 high-speed CMOS camera with a spatial. The locations of the windows within the optical access where spatially averaged chemiluminescence measurements are used for analysis in the paper are highlighted in Fig. 1. The length and width of windows W1 and W2 are 10 and 5 mm, respectively.

III. GLOBAL COMBUSTOR BEHAVIOR

Self-excited combustion instabilities were observed over a wide range of flow and flame conditions. Parametric variation of equivalence ratio (ϕ), inlet air temperature (T_{IN}), and injection velocity (u_{IN}) revealed strong sensitivity in the flame response to each parameter, which was manifested through the amplitude and frequency of the dominant unstable mode. The pressure signals measured at location C1 revealed strong spectral content within distinct bands at 360 and 720 Hz as well as two broader regions at 4.9–5.4 and 5.5–6.5 kHz. The phase difference between pressure fluctuations measured at sensor locations C1, C2, C3, and C4 was used to infer the mode orientation within the combustor and compare with computed estimates (Sec. II B and Appendixes A–D). It was determined that the 360 and 720 Hz frequencies correspond to the first longitudinal (1L) and second longitudinal (2L) modes of the combustion chamber, respectively, while the higher frequency bands were found to be oriented orthogonal (transverse) to the mean flow through the chamber. Four test cases that highlight these instability modes were selected for detailed analysis.

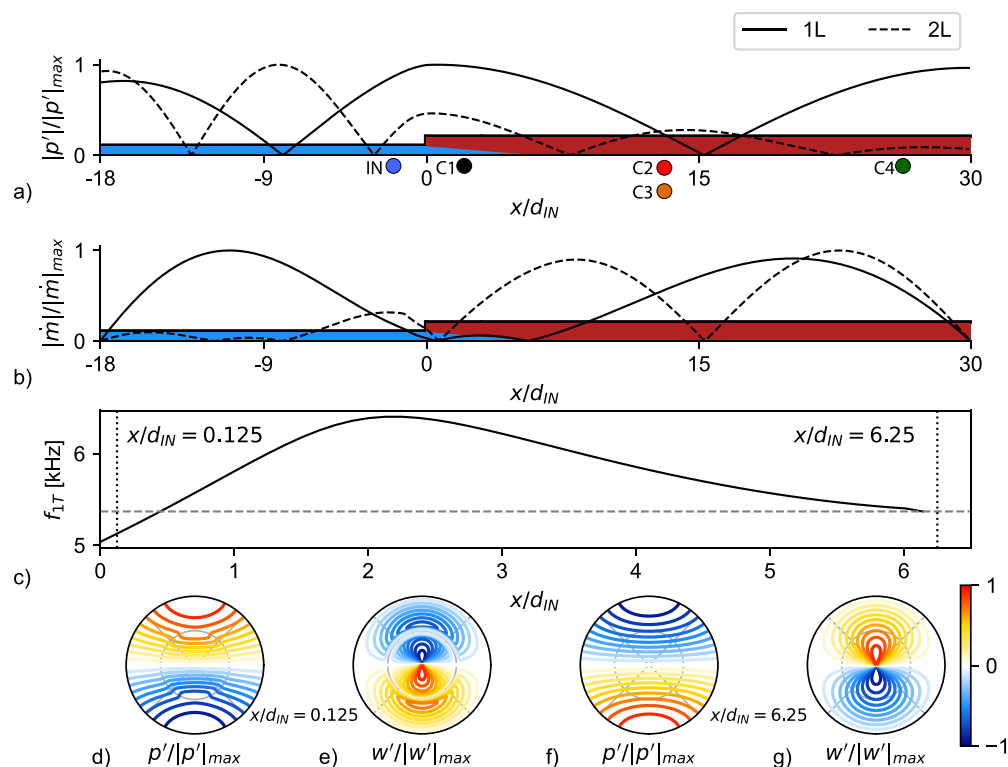


FIG. 2. (a) Pressure mode shape for fundamental (1L) and 2L modes; (b) mass flow rate fluctuations at 1L and 2L mode frequencies; (c) variation of transverse mode frequency along the length of the flame in the combustion chamber; (d) and (e) pressure (p) and velocity fluctuations (w) at the fundamental transverse mode (1T) frequency at $x/d_{IN} = 0.125$; and (f) and (g) pressure (p) and velocity fluctuations (w) at the fundamental transverse mode (1T) frequency at $x/d_{IN} = 6.25$. T_{IN} and T_C are schematically represented by blue and red shaded regions, respectively, in (a) and (b). Axial location of pressure instrumentation is highlighted on (a) for reference.

The operating conditions for these test cases, flames A–D, are listed in Table I.

Figure 3 depicts the Welch averaged power spectra of chemiluminescence intensity and pressure fluctuations within the combustion chamber for flames A–D, with shaded regions to demarcate the expected frequency bands associated with 1L, 2L, and 1T acoustic modes (see Sec. II B and Appendixes A–D). In addition to 1L and 2L, peaks corresponding to the harmonic frequencies of these modes are present on the pressure and intensity spectra for all test cases. All four conditions present pressure and heat-release fluctuations with amplitude peaks at the frequencies corresponding to longitudinal dynamics in the chamber; the 1L response is strongest for flame A, and the 2L is strongest for flame C, while flames B and D share similar amplitudes between these two modes. The distinction in flame dynamics is more

significant at the higher frequencies. Two high-frequency peaks are universally observed in the pressure signals: *HF1*, which is typically present in the range of 4.9–5.4 kHz, and *HF2*, which occurs in the range of 5.5–6.5 kHz. The relative amplitude and frequency of *HF1* and *HF2* vary between operating conditions.

To provide a summary of the behavior highlighted in Fig. 3 for flames A–D across a broader operation space, an overview of the measured pressure fluctuation amplitudes within each frequency band is shown in Fig. 4: (a) 340–360, (b) 680–720, (c) 4.9–5.4, and (d) 5.5–6.5 kHz. The velocity of the premixed NG–air flow (u_{IN}) and the adiabatic flame temperature (T_{ad} , computed from the global equivalence ratio ϕ and mixture temperature T_{IN}) were identified as the two key parameters that affected the hydrodynamics and chemical kinetics, respectively, and could be used to delineate the instability modes.

TABLE I. Summary of operating conditions for representative test cases.

Case	ϕ (· · ·)	p_{IN} (bar)	T_{IN} (K)	T_{ad} (K)	u_{IN} (m/s)	p'/p_C (%)	f_{1L} (Hz)	f_{2L} (Hz)	f_{1T} (kHz)
Flame A	0.76	7.2	764	2280	134	2.7	360	720	5.4–6.8
Flame B	0.65	6.7	720	2070	134	12.4	345	680	5.2–6.4
Flame C	0.70	6.9	623	2073	115	13.9	360	680	5.0–6.4
Flame D	0.79	7.1	617	2217	110	5.7	360	715	5.0–6.7

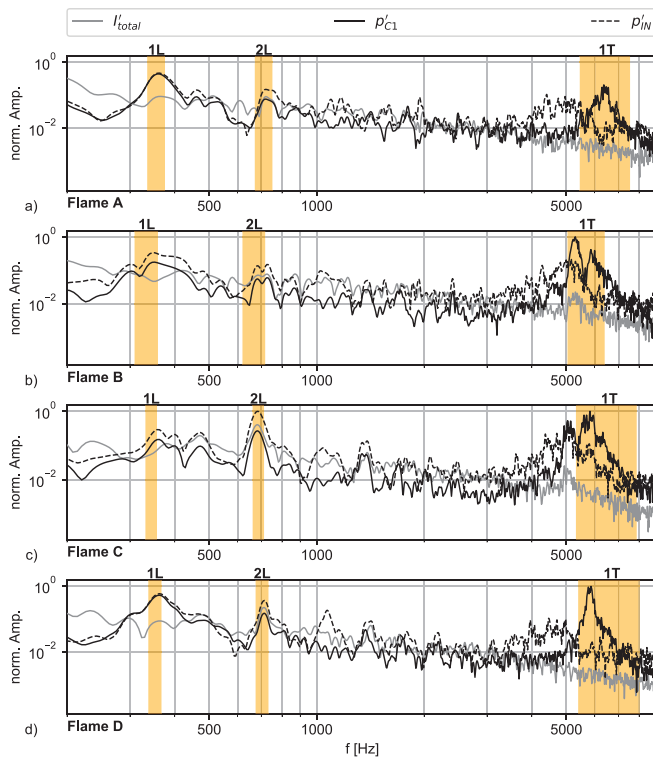


FIG. 3. Power spectra based on fluctuations in wall pressure measurements (locations IN and C1 from Fig. 1) and integrated OH* chemiluminescence intensity signal for (a) flame A, (b) flame B, (c) flame C, and (d) flame D. Shaded area represents an estimate of expected acoustic frequency for the longitudinal and transverse modes in the combustor.

Figure 4(a) shows that the 1L mode instability is largely insensitive to operating conditions, with pressure fluctuation amplitude remaining at $\leq 0.5\%$ of the mean chamber pressure throughout the operating map. Pressure fluctuation amplitudes corresponding to the 2L mode

are highest at the lowest range of temperatures and velocities tested, as indicated in Fig. 4(b). In the frequency range of 4.9–5.4 kHz (denoted HF1 henceforth), the measured amplitudes are greatest at high injection velocities and corresponding low temperatures. In the frequency range of 5.5–6.5 kHz (denoted HF2 henceforth), the measured amplitudes are highest when velocities are low or the adiabatic flame temperature is low, that is, for $u_{IN} \approx 115$ m/s and $T_{ad} < 2200$ K, which coincides with the regions of high 2L mode amplitudes.

Correlation between the reactant jet velocity (u_{IN}), the flame temperature (T_{ad}), and the amplitude, frequency, and orientation of the combustion instability observed in Fig. 4 highlights the importance of the underlying flow-field hydrodynamics and their influence of heat release perturbations. Shear layer instabilities have long been known to be a significant mechanism of coupling between heat-release and pressure oscillations in jet-stabilized flames.^{20,21,34} However, the onset, coexistence, and preferential excitation of multiple distinct instability modes in connection with these instabilities is not understood, particularly in high-pressure, high-turbulence flows with high thermal power density combustion processes.^{8,14}

IV. PRESSURE DYNAMICS

The cross-wavelet transform (CrWT) was used to characterize the phase and amplitude relationship between pressure signals measured in the inlet premixed duct and other locations throughout the combustion chamber. This approach supports identification of common dynamics throughout the combustor, in wavelet space, that are associated with the same physical process. Regions in the CrWT space that show a CrWT modulus $\sqrt{|CrWT|}$ of $P_{CrWT} = \sqrt{|CrWT|} / \sqrt{|CrWT|_{max}} > 0.75$ are extracted for high frequency dynamics (> 1 kHz) or 0.5 for low frequency dynamics (< 1 kHz). The phase difference $\Delta\phi_{CrWT}$ and frequency of common power are calculated for extracted samples, along with the amplitude weighted circular mean and variance of $\Delta\phi_{CrWT}$ at a given frequency. Figures 5(a)–5(d) provide an overview of the instability characteristics for flames A–D in the frequency range corresponding to longitudinal mode dynamics at the chamber aft (probe C4). The CrWT-based phase difference in this

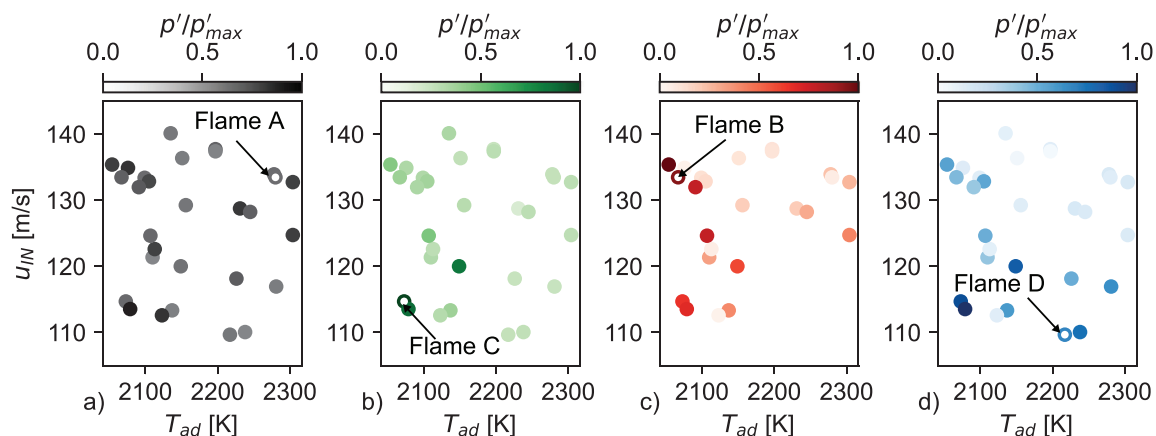


FIG. 4. Normalized pressure amplitude for modes (a) 1L (340–360 Hz), (b) 2L (680–720 Hz), (c) HF1 (4.9–5.4 kHz), and (d) HF2 (5.5–6.5 kHz) as a function of reactant jet velocity, u_{IN} , and adiabatic flame temperature, T_{ad} . Pressure amplitude is calculated from the power spectrum of the pressure measurement at location C1 and normalized by the maximum amplitude for all test cases in each respective frequency band.

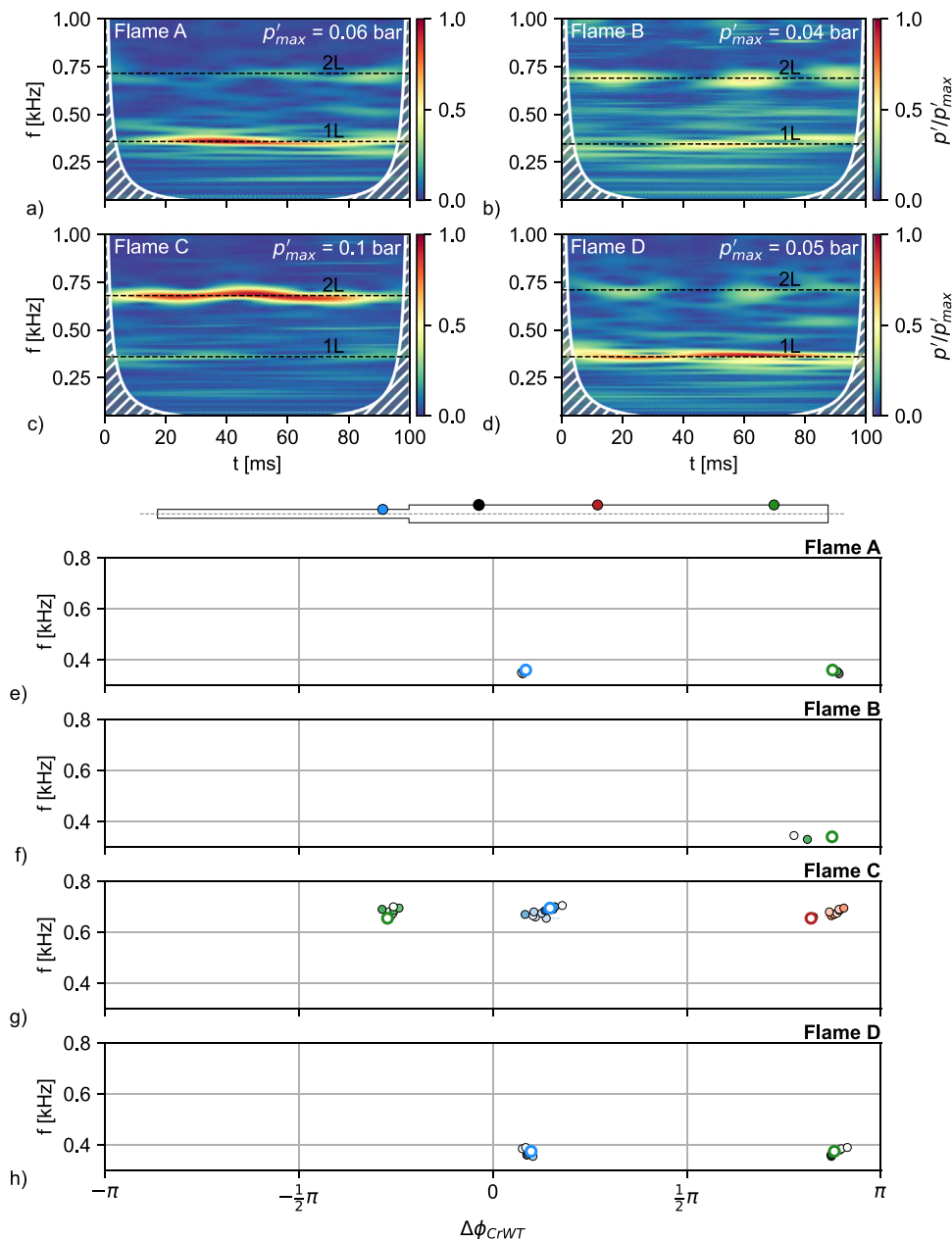


FIG. 5. (a)–(d) Wavelet scalogram of p' at C4 (COI shown as white line) and (e)–(h) CrWT based phase difference $\Delta\phi_{CrWT}$ of probes IN (blue filled circle), C2 (red filled circle), and C4 (green filled circle) relative to C1 (black filled circle) at frequencies of common power for flames A–D. Dark shading represents high common power, hollow symbol instances of maximum common power for respective probe pair.

frequency range between the chamber probe C1 and all remaining axial probes is summarized in Figs. 5(e)–5(g).

The spectrum of flame A is dominated by the 1L mode located at 360 Hz, as observed in the pressure scalogram for the chamber aft probe C4 in Fig. 5(a). Probe IN is in phase with probe C1 in this frequency band, whereas the chamber aft-end probe C4 is in phase opposition, representing a standing half-wave thermoacoustic mode in the combustion chamber with anti-nodes located near the chamber upstream and downstream boundaries. A small circular variance for these phase calculations ($\overline{Var}_\phi \approx 0$) reflects the phase-locked

dynamics in time. These measurements are consistent with results from the linear stability analysis used to design the combustor, as described in Sec. II B with mode shapes shown in Figs. 2(a) and 2(b) and complete model details given in Appendixes C and D. Although high-amplitude periods can be identified, the 1L mode does not attain a typical limit-cycle behavior as the amplitude is modulated in time. In addition, the 2L mode band is observed in the scalogram for probe C4 centered at 720 Hz, and the common power between probes here is however too low to obtain a sufficient sample for an accurate phase computation. The scalogram for flame D is similar to that of flame A,

also indicating spectral power at the 1L mode frequency. The pressure spectrum for flame C is characterized by a mode centered at 680 Hz [Fig. 5(c)]. The scalogram for flame B is characterized by general lack of coherent pressure fluctuations below 1 kHz with only intermittent low-amplitude regions at 360 Hz and 720 Hz as shown in Fig. 5(b). Although the phase relationship, $\Delta\phi_{CrWT}$, between the pressure probes

C1 and C4 shows that the bursts centered at 340 Hz correspond to the 1L acoustic mode of the chamber, it is clear from Figs. 3 and 5 that the strongest dynamics in flame B occurs at high frequencies >1 kHz.

Figures 6(a)–6(d) depict the wavelet scalogram amplitudes for flames A–D across the frequency range of 4–8 kHz, which includes the transverse instability frequencies of the combustion chamber based on

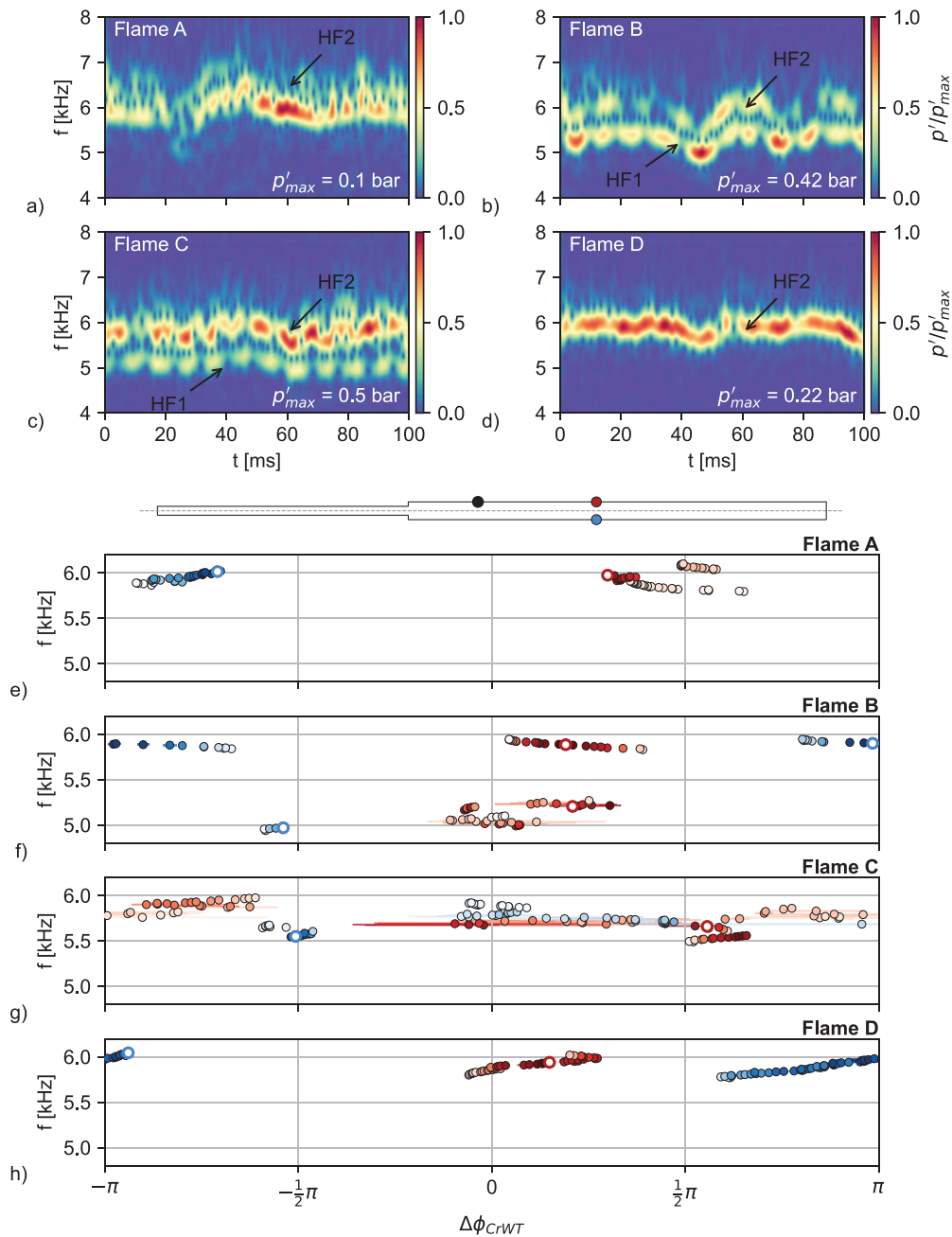


FIG. 6. (a)–(d) Amplitude based wavelet scalogram of p' at C1 and (e)–(h) CrWT-based phase difference $\Delta\phi_{CrWT}$ of C2 (red filled circle) and C3 (blue filled circle) relative to C1 (black filled circle) at frequencies of common power for flames A–D. Dark shading represents high common power, hollow symbol instances of maximum common power for respective probe pair.

the analysis described in Sec. II B and the results from Sec. III. A mode centered at 6 kHz is observed for flame A, with intermittent changes in amplitude and frequency throughout the data series. The relative phase difference between the probes C2 and C3 for this mode reveals the presence of a low-amplitude 1T mode in the chamber center, as p' at C2 and C3 are in phase opposition.

Two distinct frequency bands in the high-frequency spectrum are observed for flame B [Fig. 6(b)], a high-amplitude region centered at 5.1 kHz and a second reduced amplitude region present at 5.8 kHz. Both of these high-frequency modes lie in the range of frequencies expected for the 1T mode. The wavelet scalogram shows amplitude modulation of the 5.1 kHz mode at ~ 120 Hz. This modulation of amplitude is also observed, to a lesser extent, in the 5.8 kHz mode. Figure 6(f) shows that signals of C2 and C3 are in quadrature for the 5.1 kHz mode, whereas for the 5.8 kHz mode the signals are in phase opposition, which is consistent with the expected 1T frequency with an assumption of near homogeneous temperature field in the chamber, downstream of the flame zone (see Appendixes A and B).

Two high-frequency modes are also present for flame C centered at 5 and 5.6 kHz. In contrast to flame B, the higher frequency mode at 5.6 kHz is dominant over the 5 kHz mode at probe location C1, as depicted in Fig. 6(c). Both HF modes are highly non-stationary in frequency and show significant amplitude modulation at ~ 120 Hz similar to flame B. Buschhagen *et al.*¹⁴ correlated the presence of this ~ 120 Hz amplitude modulation with the rotation of the nodal plane of a non-stationary transverse mode about the chamber axis at ~ 60 Hz. In contrast to flame B, the lower amplitude HF mode is present throughout the sample and the modulation in amplitude at both frequencies remains in phase. Figure 6(g) shows shared dynamics between the flame zone probes at 5.5–5.6 kHz; here, the relative phase difference between C2 and C3 is $\Delta\phi_{CrWT} \approx \pi$ co-located with a maximum in common power. Var_ϕ is at a minimum for these probes in the frequency-phase space indicating phase-locked dynamics that are consistent with a 1T acoustic field. Similar to flame B, the axial sound speed distribution results in two different realizations of transverse dynamics in the flame zone and chamber center as presented in Fig. 2(g).

A single high-frequency mode centered at 5.9 kHz dominates the pressure spectrum for flame D. The WT scalogram in Fig. 6(d) demonstrates the coherent nature of this high-frequency pressure oscillation, with no apparent periodic amplitude modulations observed. The phase relationships indicate a coherent coupling between probes C2 and C3. As the mode drifts to slightly higher frequencies, the common power of C1 with the probes C2 and C3 increases, indicating a more favorable relationship between the resonant acoustic mode and the driving mechanisms. The relative phase difference between the probes C2 and C3 of $\approx \pi$ and a $\Delta\phi_{CrWT}$ of ≈ 0 and $\approx |\pi|$ for C2 and C3 relative to C1, respectively, reveal a 1T mode pressure field. The correlated frequency-phase trajectories of C2 and C3 indicate the phase-locked dynamics as the 1T mode adjusts to changes in sound speed throughout the test duration. The absence of periodic amplitude modulations for this flame condition suggests that the 1T mode pressure node plane is relatively stationary compared to flames B and C.

V. FLAME DYNAMICS

To determine the level of flame response to the chamber acoustics described in Sec. IV, OH* chemiluminescence intensity fluctuations are evaluated using the spatial average of the recorded images

$$I' = \frac{1}{mn} \sum_{x,y}^{m,n} I'_{x,y}. \quad (1)$$

Figure 3 depicts the spectra computed from a 100-ms times series sampled simultaneously with the pressure measurements presented in Secs. III and IV. The I'_{total} spectrum of flame A indicates combustion response at the 1L and 2L modes at 360 and 720 Hz, respectively. The 1T mode identified in the C1 pressure spectrum in Fig. 6(a) however shows no apparent coupling with the flame in the field of view (FOV), indicating that any interaction with the chamber acoustics must occur farther downstream. In spite of flame response at 1L and 2L modes, the I' spectrum for flame B is dominated by oscillations at 5.3 kHz, similar to the observation in the pressure spectrum [Fig. 3(b)]. The flame C emission spectrum indicates coupling of pressure and flame emission at multiple modes, where the highest energy mode is found at 680 Hz, corresponding to the 2L mode of the combustion chamber. Additionally, a 5 kHz mode is observed to alter the flame emissions. In contrast to that, the dominant 6 kHz mode in the pressure spectrum of flame C does not couple with the flame in the FOV, similar to the observations made for flame A. The I' spectrum of flame D indicates no coupling with the 6 kHz mode in the FOV, which was found to dominate the pressure spectrum at C1.

To gain insight into the spatiotemporal coupling of the flame emissions and chamber pressure field, another wavelet transform-based analysis is performed. For this purpose, the flame emission signal is integrated over the entire FOV as well as spatially limited to the windows W1 and W2, defined in Fig. 1. To directly correlate the intensity signals to the pressure field, the C1 and IN probe signals are down sampled to the imaging frequency of 50 kHz and a cross-wavelet transform-based phase relationship between p' and I' is computed. Similar to the WT pressure analysis, only valid samples from the CrWT are considered for a phase difference calculation for which $P_{CrWT} > 0.15$ and 0.8 for longitudinal and transverse dynamics, respectively.

Figures 7(a)–7(d) present the normalized cross-wavelet power of the integrated flame emission and the phase difference between the peak emission intensity and the pressure signal in the inlet duct (IN). Flame A shows common power in the 1L and 2L frequency bands, located at 360 and 720 Hz. p'_{IN} leads the 1L chemiluminescence intensity by $\approx \frac{1}{4}\pi$, resulting in periodic jet deceleration and increased heat release in the FOV due to momentum exchange between the jet and the recirculation zone in the shear layer. By contrast, at a reduced equivalence ratio ($\phi = 0.65$) and a similar T_{IN} , no direct correlation between the pressure signal and heat release is observed for flame B at the longitudinal mode frequencies. The CrWT power shows elevated regions in the 1L and 2L frequency band, but no coherent coupling is present, which is also highlighted by the stochastic phase relationships in Fig. 7(b). At the lower bound of the inlet premixed reactant temperature $T_{IN} \sim 620$ K studied here, flame C shows a strong correlation with the 2L mode at 690 Hz in Fig. 7. In this case, the I' signal lags p'_{IN} by $\approx \pi$. With increased equivalence ratio and comparable T_{IN} condition (flame D), the general flame shape remains similar, but the common power of the heat release rate fluctuations (I') with the pressure fluctuation amplitude is significantly diminished, without a change in phase between the two. This can be observed in the case of flame D as shown in Fig. 7(d).

The normalized cross-wavelet power for the OH* chemiluminescence intensity fluctuations in window W1 and the

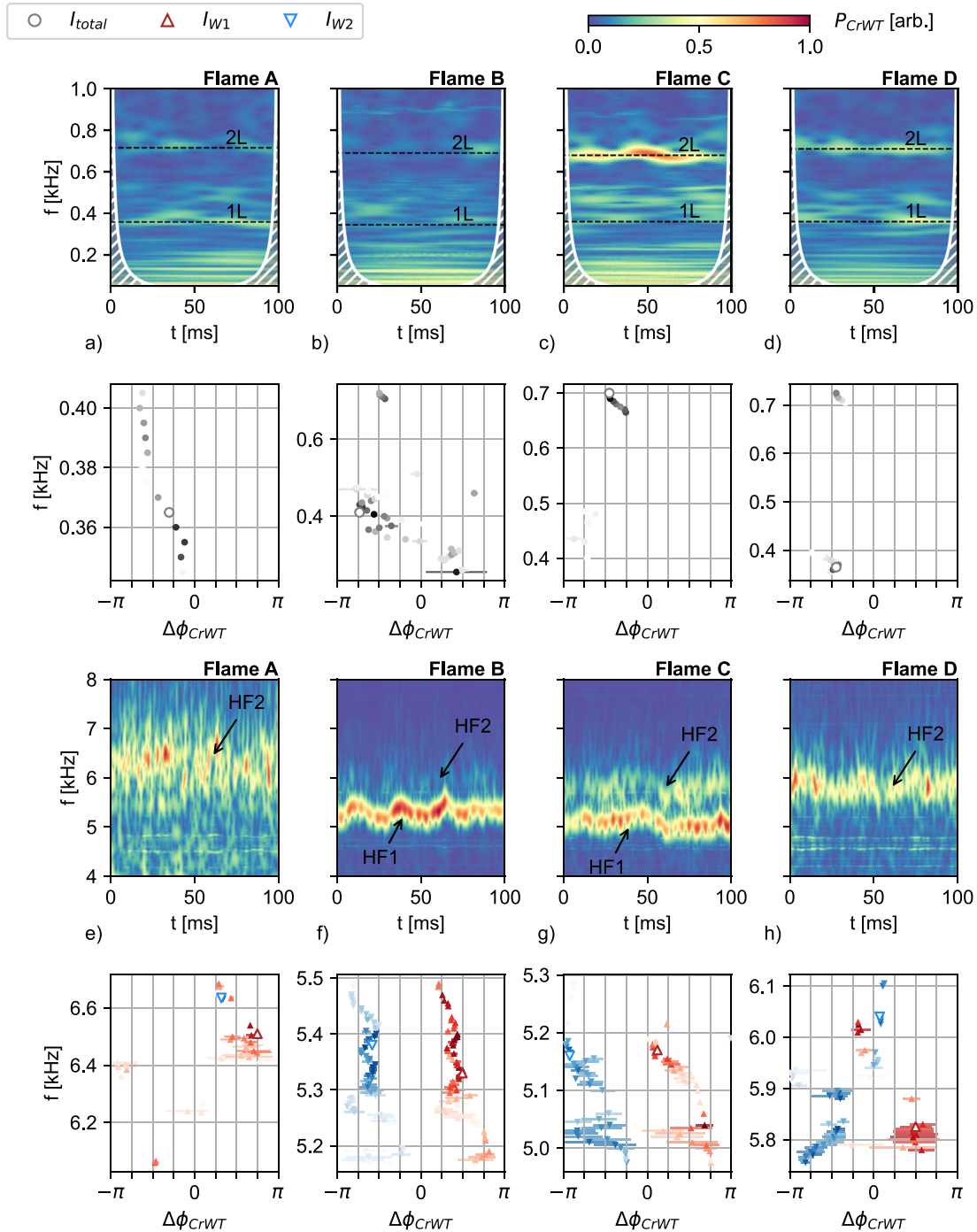


FIG. 7. Cross-wavelet scalogram of I' integrated over the FOV vs p'_{IN} (a)–(d) and W1 vs p'_{C1} (e)–(h) with CrWT-based phase difference of integrated I' for different windows relative to p'_{IN} (a)–(d) and p'_{C1} (e)–(h) at frequencies of common power.

corresponding phase difference between the emission signals of windows W1 and W2 and pressure signal at probe C1 for all four flames is shown in Figs. 7(e)–7(h). The CrWT scalogram for flame A indicates a weak correlation and inconsistent phase difference in the

≈ 6 – 6.5 kHz frequency range resulting in low combustion instability amplitude at this frequency. By contrast, a strong I'_{W1} and I'_{W2} correlation with the HF1 mode is observed for flame B at probe C1. The W1 and W2 signals are in phase-quadrature ($\Delta\phi_{CrWT} = \pm\pi/2$) with the

pressure signal at C1, which also implies that the I' in the upper and lower half of the chamber are phase opposed, as the relative phase difference between W1 and W2 is $\Delta\phi \approx \pi$. These phase relationships are consistent with a non-stationary 1T mode for which the mode nodal line circumscribes the chamber axis at 60 Hz.¹⁴ As the 1T node plane is located normal to the FOV, p' and u' associated with the mode act parallel to the FOV and the flame response/coupling with the acoustic field is observable as the flame brush undergoes strong transverse displacement resulting in high-amplitude $I'_{W1,W2}$ at $\Delta\phi_{W1-W2} = \pi$. In these instances, the 1T nodal line is located at the pressure probe C1, resulting in low-amplitude oscillations at the 1T frequency shown in Fig. 6 and discussed throughout Sec. IV. A nodal line orientation parallel to the FOV results in a reduction of I' in W1 and W2 and $\Delta\phi_{W1-W2} \approx 0$, as the transverse velocity and pressure oscillations now act normal to the FOV. The phase quadrature between $I'_{W1,W2}$ and p'_{C1} results from instances where the 1T mode transitions between these two extrema and the angle between FOV and nodal line approaches 45° .

The CrWT scalogram for flame C in Fig. 7(g) indicates a flame coupling between the flame and the acoustic field at both HF1 and HF2 frequencies. However, the phase relationship between emission and pressure signals is only determined for the HF1 mode, due to insufficient CrWT power in the HF2 band. A similar behavior compared to flame B is observed, where $\Delta\phi_{CrWT} \approx \pm\pi/4$ for W1 and W2 and a relative phase difference of $\Delta\phi_{W1-W2} = \pi$. Flame D shows only a weak correlation with the HF2 mode for which an incoherent band of common power is observed in Fig. 7(h). The corresponding $\Delta\phi_{CrWT}$ for W1 and W2 again indicates phase-quadrature with p'_{C1} and a relative phase opposition $\Delta\phi_{W1-W2} \approx \pi$ at 5.8 kHz; however, the large variance of the circular means does not allow for a conclusive phase analysis here.

A. Spectral proper orthogonal decomposition (SPOD)

Spectral proper orthogonal decomposition (SPOD) is utilized to visualize the spatiotemporal relationship between pressure (p') and flame intensity (I') fluctuations. It provides a robust means of identifying and tracking dominant coherent structures and their dynamics from the OH^{*}-chemiluminescence images in the frequency domain. The algorithm described by Towne *et al.*⁴⁶ is used to decompose the emission field into orthogonal modes in space and time. 10 000 mean subtracted images of flame emission are included in the computation spanning 200 ms of the overall test duration, where each emission ensemble includes the 100 ms pressure samples analyzed for each flame condition. This ensemble length is sufficient to study ≈ 24 cycles of the amplitude modulation of the I' at the HF1 and HF2 modes that occurs at ≈ 120 Hz and thus represents the lowest frequency of interest. The resulting frequency resolution in the SPOD analysis is 20 Hz based on 5 image blocks (Hamming Window) with 50% overlap.

Figure 8 and 9 include the energy spectra for the first and second SPOD mode ensembles indicated as E_0 and E_1 , respectively, for flames A–D. The pressure spectrum at probe location C1 is included for comparison, and all spectra are normalized by their respective maximum power. Both SPOD mode spectra for flame B are dominated by a mode at the HF1 frequency and its first harmonic as observed in Fig. 8(a). In addition, a lower frequency process at 120 Hz is present in the E_0 SPOD spectrum. The real part of the first (E_0) SPOD modes at 120 and 5260 Hz as well as the second (E_1) SPOD mode at 5260 Hz help explain the I' dynamics of flame B previously described in

Fig. 7(a). As the 1T mode circumscribes the combustor axis in the recirculation region of the flow field (the nozzle near-field), the flame strongly engages with the non-stationary pressure/velocity field. In the 5.26 kHz SPOD mode, an asymmetric initial shear layer roll-up is seen to couple with the 1T mode, leading to the high-amplitude oscillation periods in the W1 and W2 emission windows. A concurrent displacement of the flame brush leads to a spatial asymmetry in heat release in the chamber volume about the chamber axis, supplying energy into the unsteady pressure field. As the 1T mode circumscribes the chamber center axis, the emission intensity fluctuates over a longer time-scale, which is captured in the 120 Hz SPOD mode. As the OH^{*} chemiluminescence imaging is a line-of-sight integrated measurement, asymmetric intensified light emission about the chamber axis can be correlated with a nodal line orientation normal to the optical field of view (FOV), leading to the tapered spatial region originating in the nozzle near field. This period of the 120 Hz cycle corresponds to instances when the 1T nodal line is orientated normal to the FOV. During the rotation of the 1T mode, the location of its anti-node moves out of the FOV and the flame broadens as the primary interaction between p' and I' is now inline with the imaging. These dynamics describe a highly distorted flame shape, where the conical reaction zone is contracted and the flame flattens about the 1T nodal line.

The second SPOD spectrum indicates an additional dynamic process at 5.26 kHz that underlies the major transverse motion of the flame brush. Inclined bands of high intensity are observed in the second SPOD mode at 5.36 kHz that are convected by the mean flow field. These bands correspond to the asymmetric shear layer roll-up occurring at the 1T frequency, which yields distinct toroidal flow structures (vortex rings) that interact with the reaction layer. The convection velocity of these vortex rings can be estimated based on the eight instances within the FOV as $u_{conv} = 3d_{jet}f_{HF1}/VN \approx 125$ m/s, where $VN \approx 5$ is the number of intensity bands in the FOV, which corresponds to $\approx u_{jet}$.

Flame C shows similar SPOD spectra in Fig. 8(b) compared with flame B but also indicates strong flame coupling with the 2L chamber mode as indicated by the peak at 680 Hz. The SPOD mode corresponding to this frequency indicates strong axial, symmetric flame modulations about the chamber axis (not shown here). The first SPOD modes at 120 and 5.14 kHz correspond to the same processes described for flame B. As the HF2 mode dominates the pressure spectrum, the HF1 mode is less energetic leading to less coherent flame dynamics. The high-intensity bands rapidly disintegrate downstream of a $x/d_{jet} \approx 1.5$, indicating a rapid destruction of the vortices into smaller structures compared to flame B for which these structures are present within the whole FOV.

Strong longitudinal mode coupling is observed in the SPOD spectra of flame D in Fig. 9(a). Compared with the pressure spectrum, the modes at 720, 1400, and 3100 Hz stand out in the first SPOD spectrum, which all display axial modulations in the flame emissions. The 720 Hz mode corresponds to the 2L chamber mode, where axisymmetric patterns indicate periodic intensity fluctuations in the reaction layer that are correlated with the periodic shear layer roll-up and vortex merging, that occurs further downstream in flame D (and A) compared to flames B and C. The first SPOD mode at 1.4 kHz is connected to the third harmonic of the 1L chamber mode, whereas the mode at 3.1 kHz displaying periodic axisymmetric structures that interact with the reaction layer.

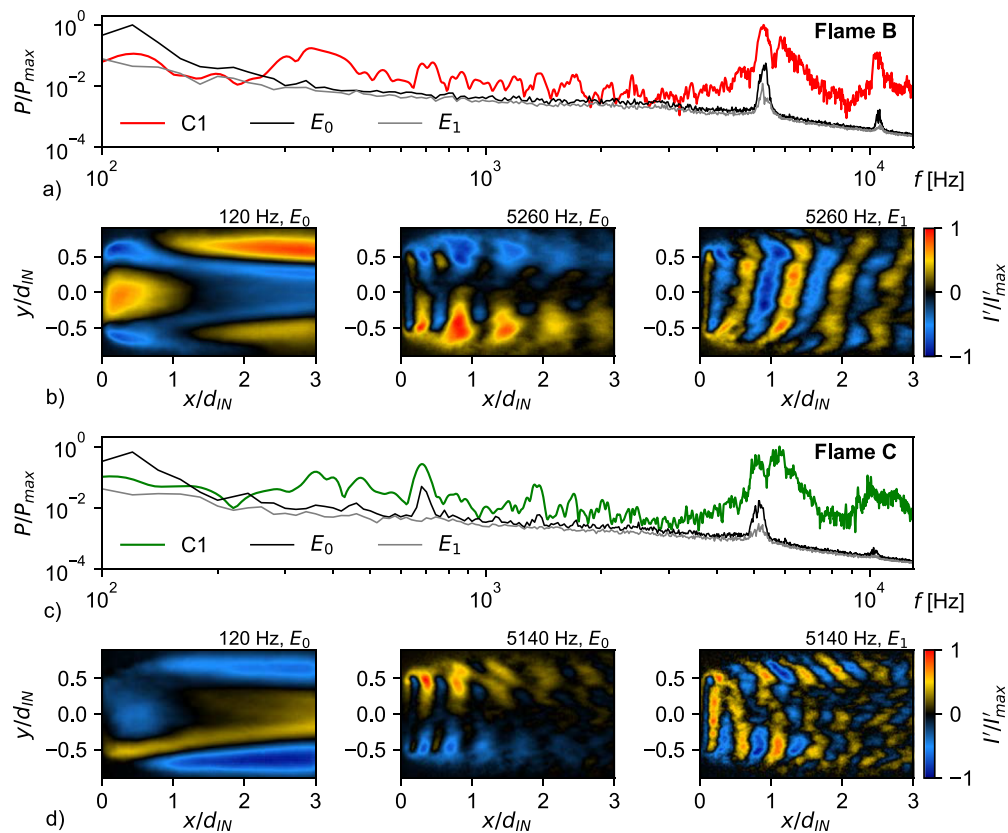


FIG. 8. (a) and (c) first SPOD mode spectra and C1 probe pressure spectrum and (b) and (d) selected SPOD modes for flames B and C. The real part of the modes is shown $\text{Re}(\Psi_{f,k})$, where k is the SPOD mode number and f the mode frequency.

VI. LINEAR STABILITY ANALYSIS OF BASE FLOW

Flames A–D manifest a complex interplay of flow and flame dynamics with varying operating conditions as seen in the SPOD results. Longitudinal and (non-stationary) transverse acoustic modes are directly observed from experimental measurements and characterized through analyses in Secs. IV and V. A quasi-one-dimensional axial linear stability analysis is used to analyze the acoustic eigenmodes of the combustor using reconstructed density, velocity, and temperature fields of the base flow. As depicted in Fig. 3, good agreement between the computed and measured frequencies is observed in both the flow and the flame.

Heat-release oscillations modulated by shear layer instabilities in the flame couple with axial acoustic modes of wavelength $\lambda_{nL} = n\pi/l_{CC}$, where n is the mode number and l_{CC} is the length of the combustion chamber. To assess the shear layer receptivity to these wavelengths, a local temporal stability analysis of the base flow radial profiles (see Appendix A) extracted in the range of $x/d_{IN} = [0, 3]$ with axial increments of $0.125d_{IN}$ is conducted. The generalized eigenvalue problem formulated in Appendix B is solved for the assigned wavelength $\alpha = \pi/l_{CC}$, and the shear layer receptivity to the 1L mode wavelength is evaluated in the optical access of the experiment ($x/d_{IN} < 3$).

The solution to the generalized eigenvalue problem indicates the presence of a neutral eigenmode (near zero growth rate) of the shear layer for the axial wave number $\alpha = n\pi/l_{CC}$. The model assumes an

infinite span in the axial directions at each instance of the computation. The normalized magnitudes of T' , u' , and v' eigenvectors at each axial position in the field of view (FOV) are shown in Figs. 10(b)–10(d). This reconstruction provides a qualitative representation of the shear layer response to the 1L mode wavelength α . The u' amplitude is highest in the recirculation zone as expected, as it expands and contracts periodically. Fluid transport from the reactant jet and the recirculation zone into the reaction layer is observed to generate temperature fluctuations T' that intensify in two distinct bands bounding the reaction layer trajectory. Increased radial velocity perturbations v' regions exist in the FOV, indicating periodic fluid exchange over the reaction layer between reactant jet and the recirculation zone. Figure 10(a) indicates that the operating conditions of Flame A have the highest likelihood that the inherent shear layer eigenmode frequencies of the base flow correspond to the 1L acoustic mode in the chamber. Conversely, departure in the response of the shear layer instability to the 1L frequency is observed for flames B–D in the region $x/d_{IN} \leq 3$.

To assess the general stability characteristics for flames A–D, a temporal analysis is conducted. For a given real-valued wavelength $\alpha \in [50 - 490] \text{ 1/m}$ the generalized eigenvalue problem is solved and perturbation modes with growth rates of $\omega_i > 1 \text{ rad/s}$ are extracted. Figure 11(a) shows a representative eigenspectrum, and only solutions with $|\omega_r| < 20 \text{ kHz}$ are shown. The eigenvalues along the ω_r axis represent the continuous spectrum of the dispersion relation, and two

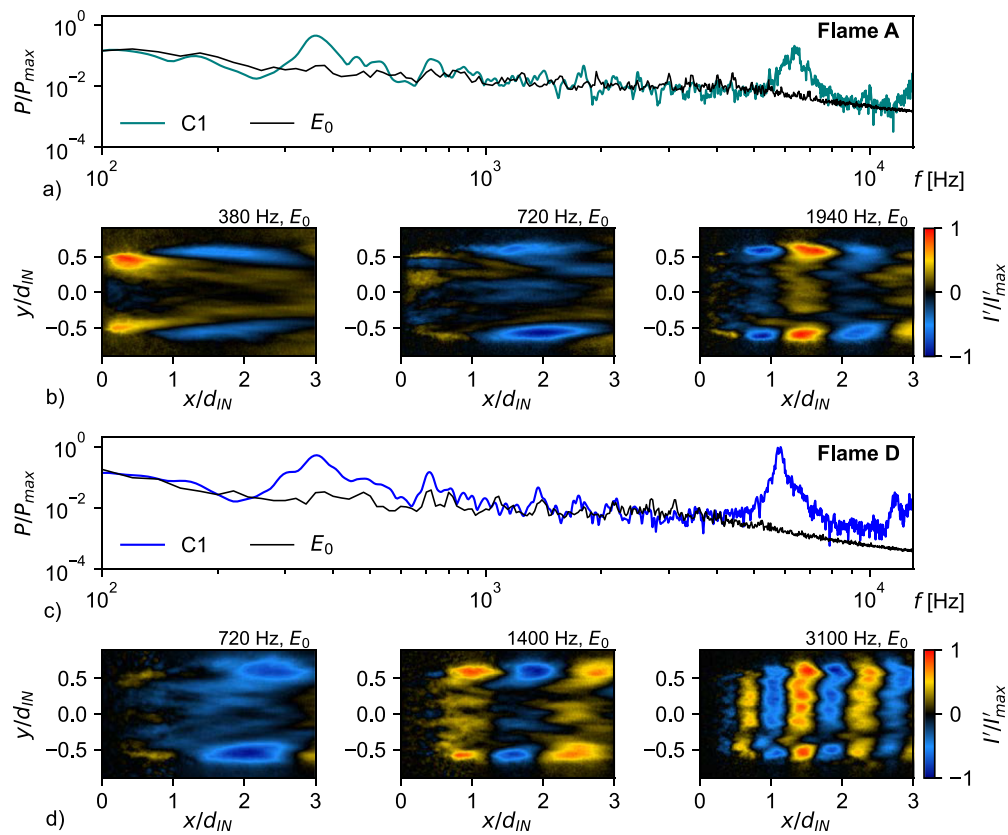


FIG. 9. (a) and (c) first SPOD mode spectra and C1 probe pressure spectrum and (b) and (d) selected SPOD modes for flames A and D. The real part of the modes is shown $\text{Re}(\Psi_{f,k}^*)$, where k is the SPOD mode number and f the mode frequency.

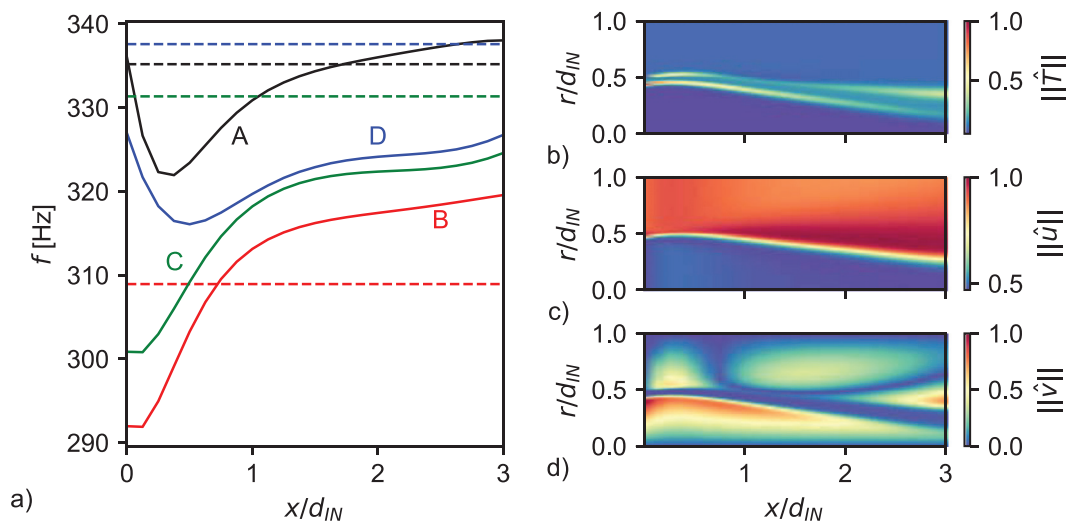


FIG. 10. (a) Response of flames A–D at the shear layer to the 1L axial chamber wavelength $\alpha = \pi/l_{CC}$. Dashed lines (---) mark the fundamental longitudinal mode for each flame. (b)–(d) Mode reconstruction of $\|\vec{T}\|$, $\|\vec{u}\|$, and $\|\vec{v}\|$, respectively, where $\|\vec{A}\| = |\vec{A}'|/|\vec{A}'|_{max}$ and \vec{A} is the quantity of interest.

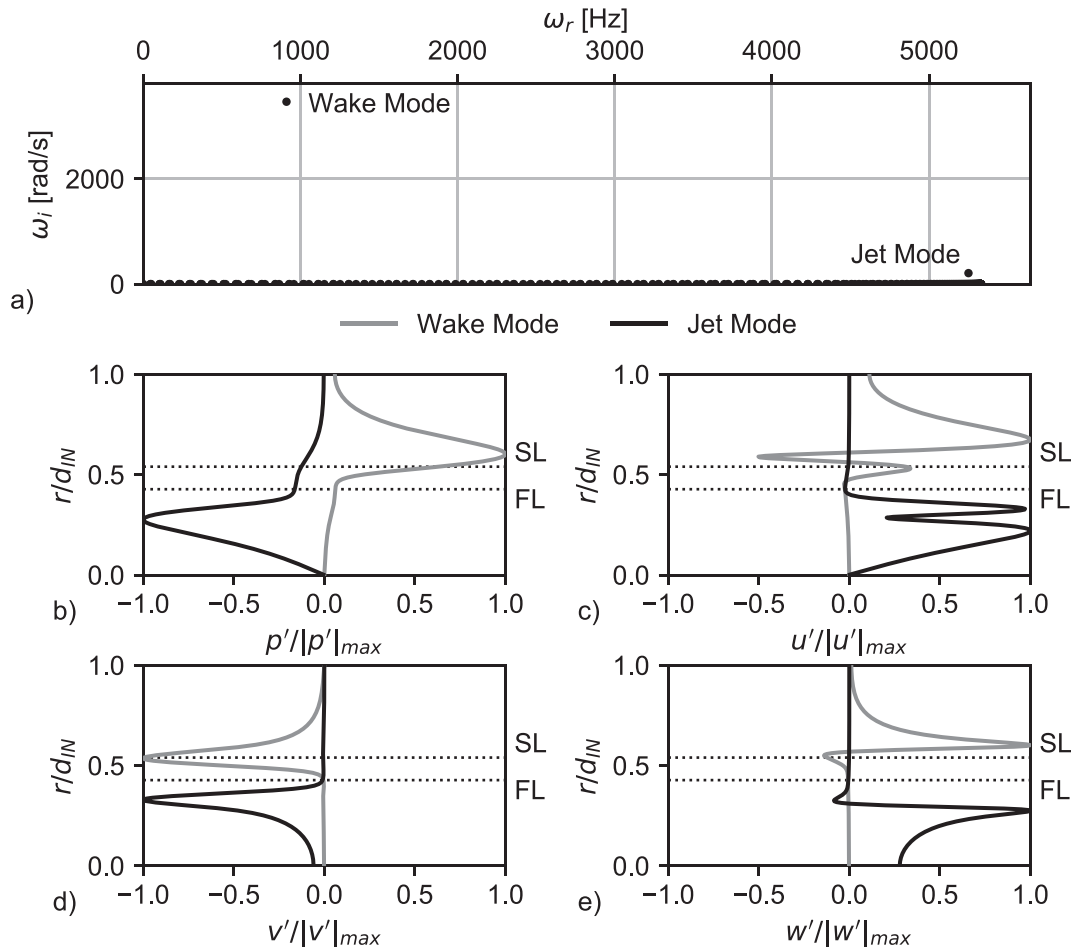


FIG. 11. (a) Eigenvalue spectrum of temporal LSA, (b) p' , (c) u' , (d) v' , and (e) w' profiles for flame B with $N = 250$, $\alpha = 250$ 1/m, $m = 1$, $x/d_{IN} = 1$. Shear layer and flame location indicated with SL and FL, respectively.

solutions are observed that are associated with convectively unstable modes, which are subsequently referred to as the *wake mode* and *jet mode*. The associated pressure and velocity eigenvectors of these modes are presented in Figs. 11(b)–11(e). The wake mode is most active in the proximity of the shear layer, identified by the location of the profile extremum adjacent to the highest velocity gradient at the shear layer centerline denoted by SL. The jet mode is mostly confined to the reactant jet core for which the maximum amplitude of all perturbation quantities develop at a location below the reaction layer. The pressure profiles for both modes indicate interaction between the mixture jet and the recirculation zone, whereas the velocity perturbations are contained within each associated region.

Figure 12 provides an overview of the wake mode stability characteristics for flames A–D over a 120-mm axial span with an azimuthal wave number of $m = 0$. The wake mode for the flame A shows a broadband receptivity throughout the initial flame zone and coupling with the longitudinal acoustic mode frequencies. High growth rates are observed at the jet exit plane ($x/d_{IN} = 0$), where the parabolic upper bound of the map to $x/d_{IN} = 1$ is attributed to the limited

axial wave number range ($\alpha \leq 490$ 1/m) studied in this work. With increasing axial distance from the jet exit plane, the growth rates decrease to a steady amplitude. The lower α bound shows negative frequencies and indicates upstream traveling waves. The preferred wake mode frequencies reside in the co-flow region ($\omega_r > 0$ Hz). Flame D shows similar characteristics as shown in Fig. 12(d). A stark contrast for the wake mode behavior is seen for flames B and C in Figs. 12(b) and 12(c). Reverse flow perturbations at low frequencies are preferred within the region $0 < x/d_{IN} < 0.6$, where flames B and C show frequencies of -80 and -275 Hz at α values of 200 and 490 1/m, respectively. The growth rates are significantly lower in the near field of the sudden expansion compared to flames A and C, before it attains a maximum value at $x/d_{IN} \approx 1$. Downstream of this region, the wake mode behaves similarly for all flames. These trends are consistent for both azimuthal wave numbers. For all flames, the high growth rate regions of the wake mode resides in a band that is compatible with the first two longitudinal chamber acoustic modes and any perturbation within that frequency band yields a spatially growing disturbance downstream. This convectively unstable mode has the potential to

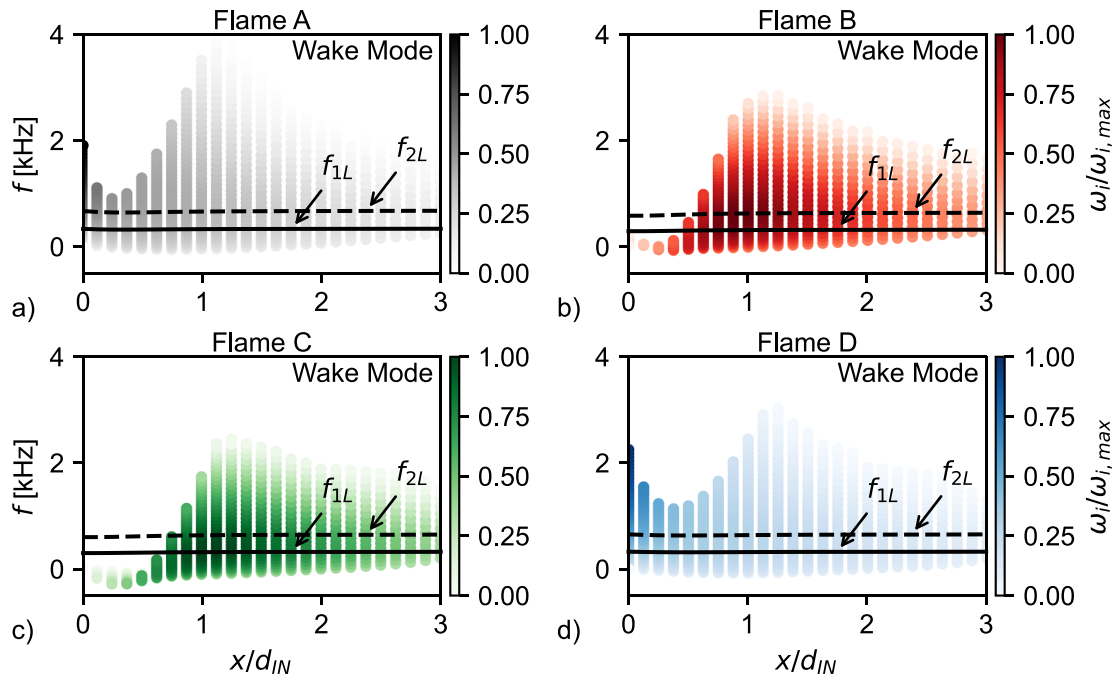


FIG. 12. Wake mode stability map for flames A–D computed with $m = 0$ within the axial range of $x/d_{IN} = 0 - 3$ overlaid with computed 1L and 2L frequencies. Mode growth rate ω_i indicated by shading of data points.

couple with the combustor acoustic mode through unsteady heat release that is generated by the interaction of hydrodynamic perturbations and the reaction layer.

The jet mode is associated with fluctuations of the premixed reactant jet injection and is associated with higher frequencies than the wake mode, closer to the transverse acoustic eigenmodes of the combustor. Figure 13 provides an overview of the jet mode stability characteristics for $m = 1$. A maximum temporal growth rate within the axial range of $x/d_{IN} = [0, 1]$ is observed for all flames. This maximum is located closer toward the injector exit plane for flames B and C compared with A and C, and is correlated with the region of decreased receptivity of the wake mode. The jet mode is receptive to perturbations at 1T and 2T frequencies for which the maximum growth rates reside in the near field of the sudden expansion and continuously decreases in the downstream direction, consistent with the relaxation of the base flow gradients. These trends are consistent with both azimuthal wave numbers within the axial range $x/d_{IN} = [0, 2]$. Downstream of that region the base flow is unable to support the axisymmetric jet modes. The helical jet mode receptivity steadily decreases until $x/d_{IN} = 2.25$ where an inflection point is observed, leading to a frequency increase toward the end of the computational domain.

The temporal stability characteristics for flames A–D are compared for the axial location $x/d_{IN} = 1$ in Fig. 14. The local maximum temporal growth rates for both modes and azimuthal wave numbers are indicated with vertical lines and horizontal lines mark the 2L and 1T acoustic mode frequencies. The jet mode reaches its maximum growth rate (highlighted by vertical (—) and (---) lines) at a frequency that corresponds to the local 1T frequency for flames B and C.

Conversely, an offset between the 1T frequency and location of maximum jet mode growth rate is observed for flames A and D.

Figures 15(b) and 15(d) show the highest energy SPOD modes for frequencies 720 and 5260 Hz for flames D and B, respectively. The pressure and SPOD spectra for flame D indicate prominent peaks in pressure and heat release fluctuations at frequencies corresponding to the 2L and 4L modes of the chamber at 720 and 1400 Hz. At the 720 Hz mode, axisymmetric distribution of periodic intensity fluctuations in the reaction layer are observed that can be correlated with the periodic shear layer roll-up process. Conversely, an asymmetric shear layer roll-up is observed for the SPOD mode at 5.26 kHz at the injector exit, resulting in high-amplitude oscillation periods in the W1 and W2 emission windows observed in Fig. 7(f). The transverse displacement of the flame brush leads to a spatial asymmetry in heat release in the chamber volume about the chamber axis, supplying energy into the unsteady pressure field. These flame dynamics are consistent with the presence of a 1T instability in the flame zone.

Figures 15(a) and 15(c) show the axial wavelength λ_x of the wake and jet modes with azimuthal wave numbers of $m = 0$ and $m = 1$ for the 2L and 1T mode frequencies over the axial span of the computational range. Shown is the mean value of an LSA frequency band, which is bounded by $\Delta f = |f_{LSA} - f_x|/f_x < 0.1$. The axial wave lengths λ_x for flames A and D in Fig. 15(a) show a minimum at $x/d_{IN} \approx 0.3$ and continuously increase toward the end of the domain reaching a maximum at 1.8–2, which correlates well with the indicated λ_x of the 2L SPOD mode of flame D. λ_x for the flames B and C jet mode in contrast decreases from a maximum located in the sudden expansion near field toward a minimum located at $x/d_{IN} \approx 1.7 - 2$, and shows the profile inflection corresponding to the stability maps

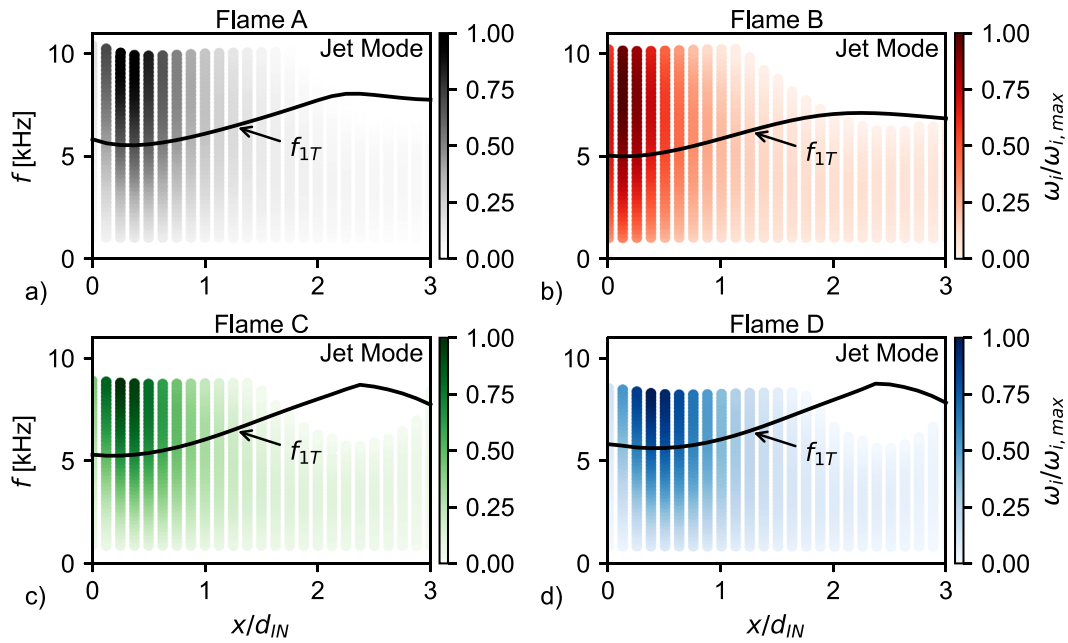


FIG. 13. Jet mode stability map for flames A–D computed with $m = 1$ within the axial range of $x/d_{IN} = 0 - 3$ overlaid with computed 1T frequency. Normalized growth rate, ω_i , for the mode is indicated by shading of data points, with higher value indicated with a darker shade.

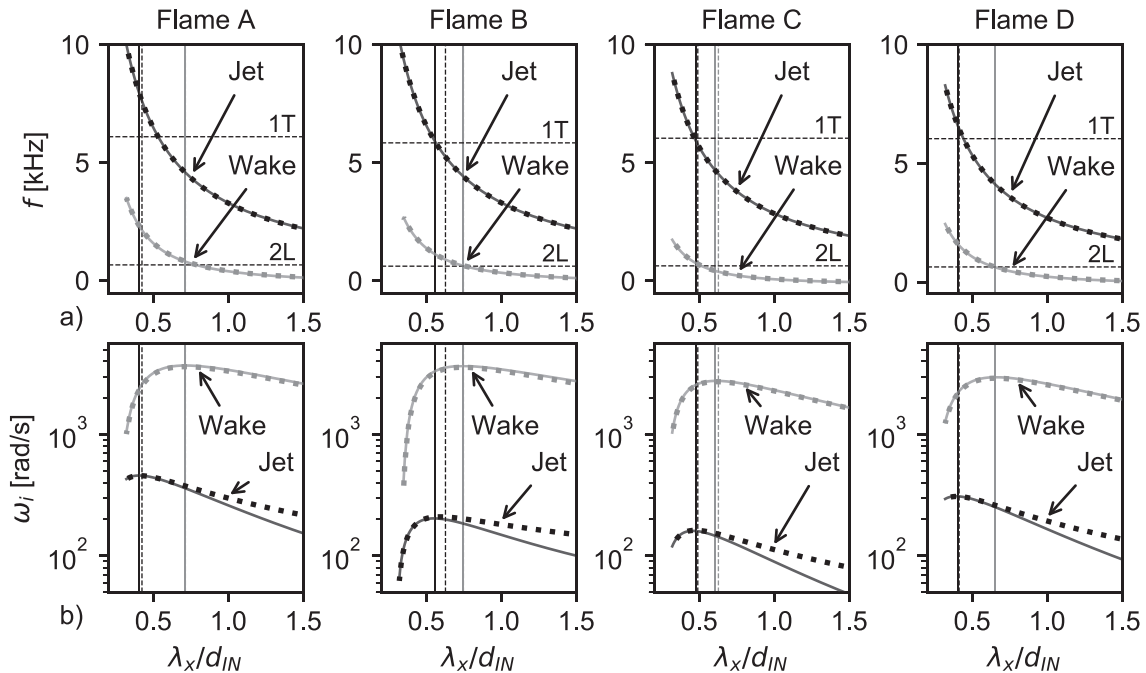


FIG. 14. Perturbation modes extracted from temporal stability analysis at $x/d_{IN} = 1$: (a) frequency and (b) temporal growth rate ω_i as a function of normalized axial wavelength of the unstable mode, λ_x/d_{IN} of convectively unstable modes for flames A–D. Vertical (—) and (---) lines mark $m = 0$ and $m = 1$ maximum of ω_i . Mode trajectories for $m = 0$: (—), $m = 1$: (□).

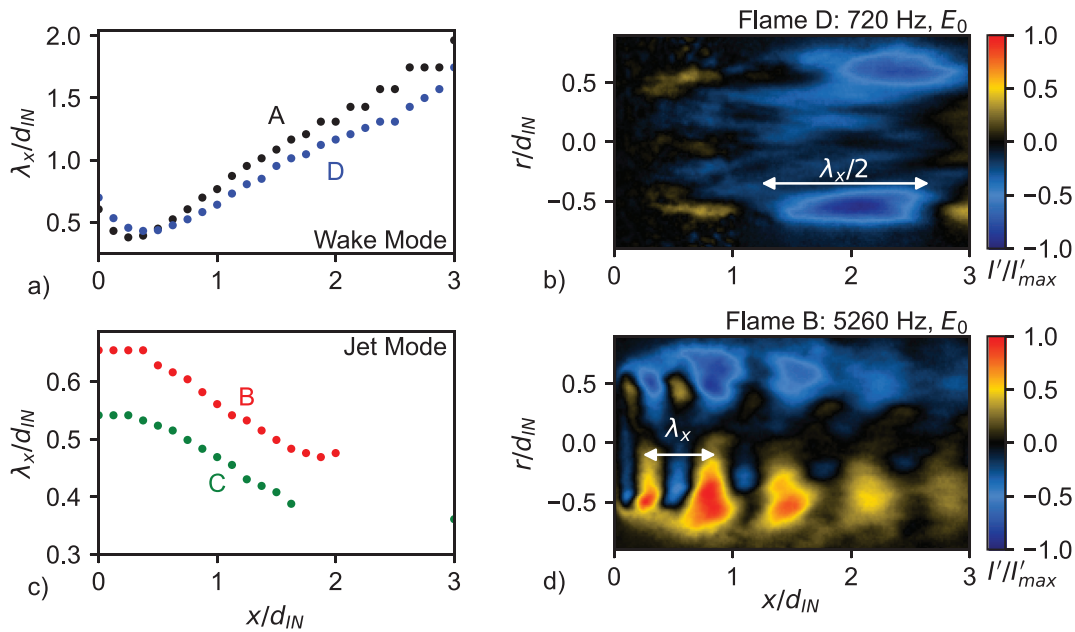


FIG. 15. Axial wavelength trajectories of LSA modes at the 2L and 1T chamber modes for (a) the wake mode with $m=0$ and (c) the jet mode with $m=1$. Highest energy ranked SPOD modes from OH^+ -chemiluminescence snapshots for (b) flame D at 720 and (d) flame B at 5.26 kHz.

shown in Figs. 13(b) and 13(c). The trajectories of the jet mode wavelengths for flames B and C show good qualitative agreement with the SPOD modes found at the 1T frequencies of 5.26 and 5.14 kHz from the experiment. The predicted jet mode frequency at $x/d_{IN} = 1$ for flame B is 5.25 kHz with an axial wavelength $\lambda_x/d_{IN} = 0.63$. Flame C has a preferred jet mode frequency of 5.45 and 4.88 kHz at $x/d_{IN} = 1.125$ and 1.25, respectively, with the associated axial wave lengths $\lambda_x/d_{IN} = 0.52$ and 0.58. Both comparisons demonstrate good agreement of the model results with the experimental observations.

A volumetric reconstruction of the flame B jet mode with azimuthal wave numbers $m=1$, $m=-1$, and their superposition is

shown in Fig. 16. For reconstruction, a constant axial wavenumber of $\alpha = 250 \text{ 1/m}$ or $\lambda_x/d_{IN} = 0.63$ is chosen, which represents the α that corresponds to the measured HF1 frequency for flame B and the mean for the α trajectory in the region $x/d_{IN} = [0, 1]$ [Fig. 15(c)]. In order to compose the volumetric field from the axially discrete spatial LSA, the angular position of the maximum amplitude in each polar pressure field $p'_{max}(x)$ was determined and subsequently clocked in the axial direction. The angular position of $p'_{max}(x)$ is then determined by $\theta_p(x) = \alpha x$ with the initial condition $\theta_p(x) = 0$. All other polar fields of the perturbation quantities are clocked according to p' . The resulting cylindrical perturbation fields are then transformed into Cartesian coordinates, and a linear interpolation is performed on a 101×100

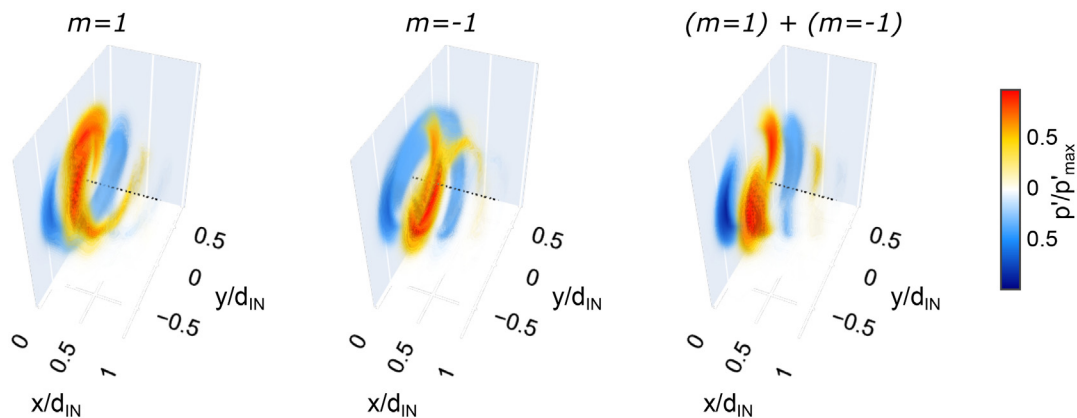


FIG. 16. Jet mode pressure field reconstruction for flame B with azimuthal wave number $m=1$, $m=-1$ and their superposition. Axial wave number is $\alpha = 250 \text{ 1/m}$, and the axial range is limited to $x/d_{IN} = [0, 1]$ for clarity.

grid spanning the lateral and axial range of $y/d_{IN} = [-1, 1]$ and $x/d_{IN} = [0, 2]$, respectively.

The two azimuthal modes, $m = +1$ and $m = -1$, indicate helical structures that circumscribe the jet potential core, with their maximum amplitudes bounded by the flame trajectory. The perturbation amplitude of these modes rapidly decreases axially and is most prominent in the near field of the sudden expansion ($x/d_{IN} < 1$). As both helical modes have the same likelihood to exist especially in a non-swirling jet for which no preferential rotation direction is present, a superposition of both modes is likely to occur. The pressure field of this combined jet mode features a nodal plane, which is located within XZ plane in the reconstruction corresponding to the solutions for $\theta = [\pi/2, 3\pi/2]$ in the radial LSA. In the nodal plane, the two modes interfere resulting in a low amplitude, whereas an amplification occurs in the perpendicular anti-nodal plane (XY plane in reconstruction) corresponding to the solutions for $\theta = [0, \pi]$. The resulting asymmetric pressure field distribution forms crescent regions that are bounded by the flame trajectory in the exterior and decrease toward the chamber centerline. The helical mode pitch hereby determines the distance between the adjacent regions of alternating pressure perturbations.

From a comparison of these three modes, it is evident that a combined azimuthal mode results in a structure consistent with the transverse mode pressure distribution observed experimentally at the entrance of the combustion chamber. The single helical modes ($m = +1$ and $m = -1$) result in perturbation of the flow field uniformly across the chamber centerline, and thus, any heat release rate fluctuations can interfere with a transverse mode due to the absence of a distinct nodal plane. By contrast, the combined azimuthal mode alters the flow field symmetrically about the anti-node, resulting in two spatially concentrated regions separated by the node plane, which

is capable of supporting observed non-stationary transverse combustion instability in the chamber.

The u' and v' fields for the combined mode in the nodal (XZ) and anti-nodal (XY) planes are shown in Fig. 17. The u' field shows an asymmetric distribution about the chamber centerline and reflects the alternating crescent pressure regions centered about the anti-nodal plane. The v' distribution is symmetric about the centerline according to the asymmetric pressure differential about the XZ plane. The u' and v' fields in the XZ plane show symmetric and asymmetric distributions about the centerline with significantly reduced magnitudes compared to the XY plane, due to the interference of the two helical $m = +1$ and $m = -1$ modes. The vorticity distribution in the two planes is computed using the axial and lateral velocity components with $\omega_z = \partial v/\partial x - \partial u/\partial y$ and $\omega_y = \partial u/\partial z - \partial w/\partial x$, where $w = v$ and $z = y$ due to the coordinate system change. The ω_z distribution in the anti-nodal plane indicates the presence of asymmetric shear layer roll-up, evident by the equally spaced stagnation points along the flame trajectory. The ω_y distribution in contrast does not show a consistent stagnation point structure, resulting from the interference of the two modes in the nodal plane.

This structure of the perturbation field yields an asymmetric shear layer roll-up about the nodal plane of the hydrodynamic mode, which, given that the chemical and spatiotemporal scales are compatible, induces an asymmetry in the flame surface distribution within the chamber. A single helical mode results in an asymmetric roll-up as well, but no nodal plane exists. Thus, the heat-release fluctuations that would arise from this mode are not compatible with the observed 1T dynamics from the experiments. The single nodal plane of the coupled hydrodynamic mode, however, is compatible and consistent with the 1T acoustic field and thus holds a large potential for self-excitation of the 1T mode in the flame zone as observed in the experimental measurements.

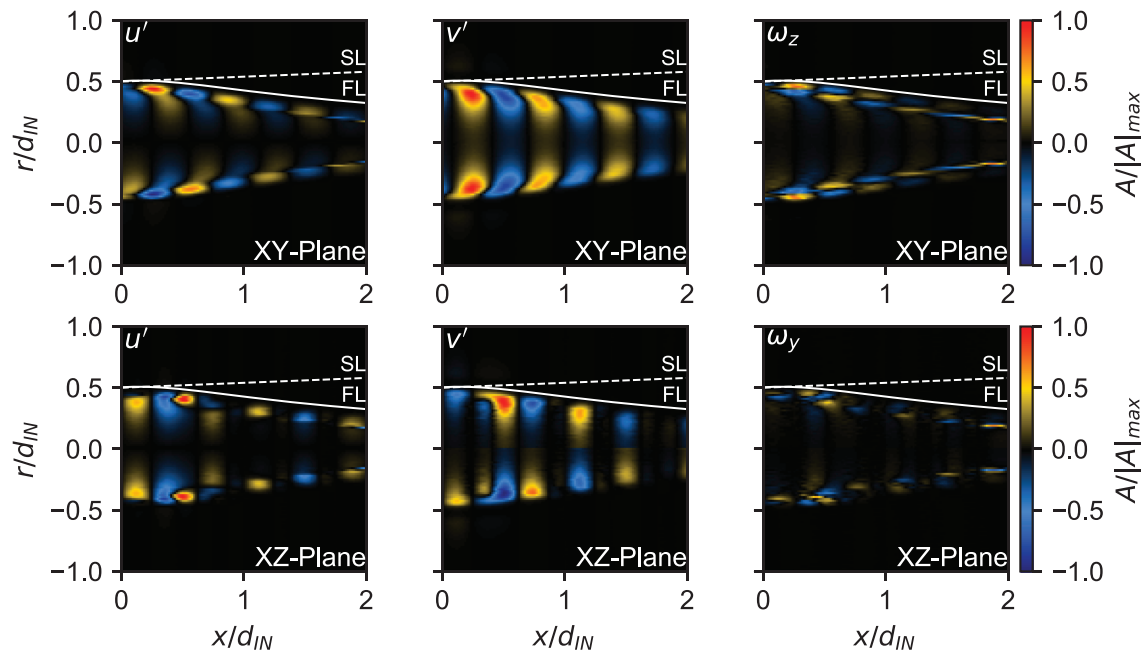


FIG. 17. Reconstructed u' , v' and vorticity fields for the combined jet mode of flame B in the XY and XZ planes. Scalar fields are normalized by their absolute maximum. Flame trajectory (FL) and shear layer centerline (SL) indicated only in upper quadrant for clarity.

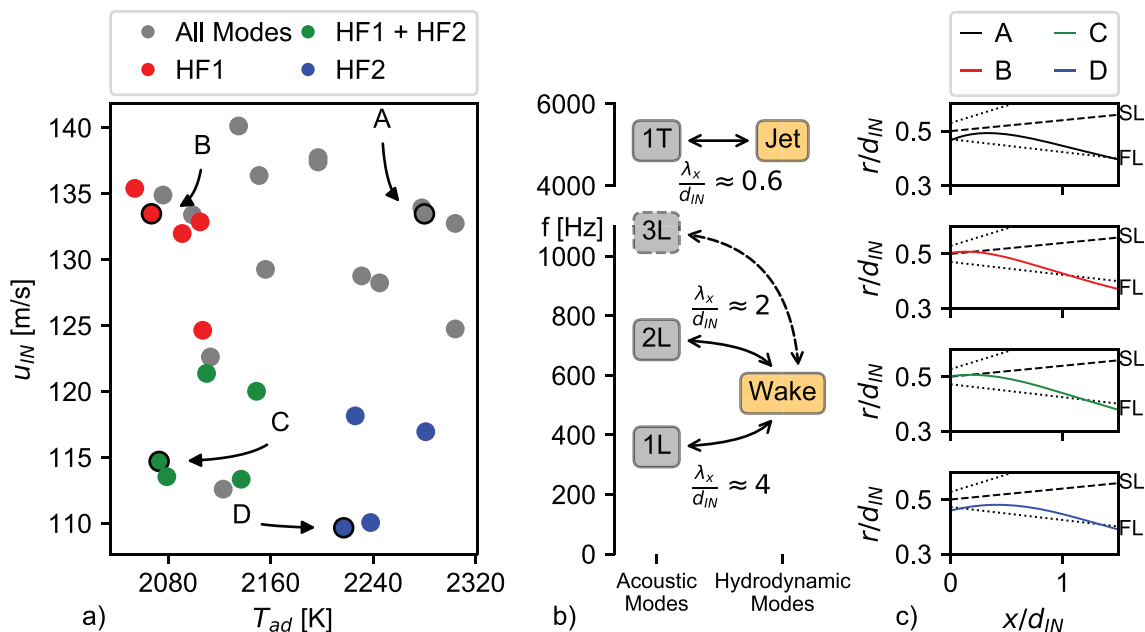


FIG. 18. Overview of multi-mode response of flames A–D: (a) multi-mode instability map in the u_{IN} vs T_{ad} operational space; (b) frequency comparison between 1L, 2L, 3L, and 1T acoustic modes, and jet and wake intrinsic hydrodynamic modes; (c) flame trajectories (FL) relative to the shear layer (SL) center, with dotted lines indicating the shear layer thickness.

VII. CONCLUSIONS

Self-excited combustion instabilities in a lean-premixed natural gas–air turbulent jet flame were investigated at high pressures ($p_C = 7$ bar) and Reynolds numbers ($Re_{jet} \sim 5 \times 10^5$). Multiple axial and transverse thermoacoustic modes were identified, with instability amplitudes varying as a function of the reactant jet velocity and the adiabatic flame temperature [as depicted in Fig. 18(a)]. Longitudinal modes (1L and 2L) were observed across the operation envelope, with pressure fluctuation amplitude levels of $p'/p_C < 9\%$. At high reactant jet velocities ($u_{IN} > 120$ m/s) and low equivalence ratios, a 4.9–5.4 kHz transverse mode instability (denoted as HF1 throughout the paper) becomes the dominant process. At low jet velocities and high equivalence ratios, a second transverse mode becomes dominant at a higher frequency range of 5.5–6.5 kHz (denoted HF2). At low equivalence ratios and low reactant jet velocities, the two transverse modes were found to co-exist within the flame zone with comparable amplitude levels.

A local linear stability analysis was performed for four down-selected test conditions (demarcated as conditions A–D in Fig. 18). A parametric study for the axial wavelength α and azimuthal wave number m revealed the presence of two modes in the base flow of this configuration, associated with the wake and jet regions. The wake mode was associated with lower frequencies of $\mathcal{O}(100)$ Hz, which are compatible with the longitudinal acoustic resonances of the combustion chamber. Flames A and D show compatible mode frequencies and growth rates throughout the analyzed axial length. The jet mode is associated with higher frequencies of $\mathcal{O}(5000)$ Hz, where it is compatible with the transverse acoustic modes of the combustion chamber. All four flame conditions support the jet mode in the region $x/d_{IN} = [0, 1]$. Flames B and C support a maximum growth rate in

the region immediately downstream of the sudden expansion, whereas the maximum growth rate for flames A and D were found further downstream. Figure 18(b) summarizes the interaction pathways between hydrodynamic and thermoacoustic modes in this burner configuration. Wavelengths extracted for the wake and jet modes at the 2L and 1T frequencies were in close agreement with the experimentally measured pressure and flame dynamics for all for flames.

The spatial location of the reaction zones was evaluated relative to the location of the jet shear layers to delineate the observation of preferential flow–flame coupling at the four flame conditions. At low flame temperatures, the reaction zone was found to be shifted radially outward, into the low-velocity regions of the flow [flames B and C in Fig. 18(c)]. At high flame temperatures, the flame was stabilized closer to the jet centerline, where higher turbulent flame speeds were supported by higher reactant flow velocities [flames A and D in Fig. 18(c)]. The turbulent flow within the flame zone provides a wide spectrum of velocity perturbations that could couple to heat release oscillations through interaction with the reaction layer. In the near injector region, this shift in heat release location relative to the underlying base flow was found to be the root cause for coupling of unstable modes within this broad hydrodynamic spectrum. These conclusions are supported by excellent agreement between the convectively unstable modes identified by the temporal LSA and the measurement of flow and flame dynamics in a self-excited, high power-density combustion instability experiment.

ACKNOWLEDGMENTS

The high-speed camera used in this work was purchased with DURIP Grant No. FA9550–16–1–0534 (PO: Dr. Chipping Li).

The authors are also grateful for the support provided by John Philo and Mark Frederick during test operations.

AUTHOR DECLARATIONS

Conflict of Interest

The authors have no conflicts to disclose.

DATA AVAILABILITY

The data that support the findings of this study are available from the corresponding author upon reasonable request.

APPENDIX A: BASE FLOW RECONSTRUCTION FOR RADIAL MODEL

The base flow for a radial linear stability analysis is assumed to be locally parallel and inviscid. Axial velocity u_0 , fluid temperature T_0 , and density ρ_0 are described by local profiles in cylindrical coordinates in order to investigate the stability of the flow at a given axial position x in the flow field. A hyperbolic tangent-based formulation is employed for the axial velocity profile and defined by:

$$u_0(x, r) = u_c(x) \left[\frac{1 - \beta(x)}{2} + \frac{\beta(x) + 1}{2} \tanh \left(\frac{1}{\delta(x)} (r_{IN} - r) \right) \right], \quad (A1)$$

where u_c is the local centerline velocity and β is the back flow ratio defined by $\beta(x) = u_{0,min}(x)/u_c(x)$.^{36,47} The width of the transition region in the profile is controlled by δ and models the shear layer width, which is assumed to increase linearly with the classical result for the round jet spread rate of $S = 0.094$ (Ref. 48) and is defined as

$$\delta(x \leq x_s) = \delta_{min} + \frac{r_{IN} - \delta_{min}}{x_s} x, \quad (A2)$$

$$\delta(x > x_s) = r_{IN}, \quad (A3)$$

where an initial shear layer thickness of $\delta_{min} = 4.9L_{IN}Re_x^{-0.5} = 0.026d_{IN}$ is assumed based on Blasius' solution to the zero-pressure gradient boundary layer thickness for pipe flow.⁴⁸ The resulting shear layer developing length is $x_s = 5.4d_{IN}$. The back flow ratio determines the velocity magnitude at the wall and is negative in the recirculation zone for $x < x_r$ and positive downstream of x_r as the mean profile slowly assumes that of fully developed pipe flow. Experimental data from Stevenson *et al.*⁴⁹ and Pitz and Daily⁵⁰ suggest a maximum recirculation velocity magnitude of 22% of the centerline velocity u_c that occurs at $x_\beta = 1.5d_{IN}$ and a shortened recirculation zone length of $x_r = 3.5d_{IN}$ compared with a non-reacting flow field. Two polynomials are formulated to describe the back-flow ratio in the recirculation zone and in the developing region as

$$\beta(x \leq x_r) = \frac{\beta_{max}}{x_\beta^2 - x_r x_\beta} (x^2 - x_r x), \quad (A4)$$

$$\beta(x > x_r) = \frac{\beta_{min}}{(x_r - x_d)^2} \left((x_r - x_d)^2 - x_d^2 + 2x_d x - x^2 \right), \quad (A5)$$

with $\beta_{max} = 0.22$, $\beta_{min} = -0.05$, and $x_d = 7d_{IN}$ as the length of the analysis domain. Stevenson showed that the centerline velocity u_c is

observed to decay farther downstream compared with a non-reacting flow field and is estimated as

$$u_c(x) = u_{in} + \frac{u_d - u_{IN}}{(x_d - x_p)^2} (x_p^2 + x^2 - 2x_p x), \quad (A6)$$

where $x_p = 3.5d_{IN}$ is the jet potential core length and $u_d = 0.88u_{IN}$ the centerline velocity at the end of the domain.⁴⁹ The radial derivative of the axial velocity is defined as

$$\frac{du_0(x, r)}{dr} = u_c(x) \left[\frac{\beta(x) + 1}{2\delta(x)} \cosh^{-2} \left(\frac{1}{\delta(x)} (r_{IN} - r) \right) \right]. \quad (A7)$$

Temperature and density fields are linearly related by the ideal gas law. With the temperature ratio $TR = T_{IN}/T_C$, where T_C is estimated by the adiabatic flame temperature T_{ad} and density ratio $DR = \rho_{IN}/\rho_C$, the base flow temperature and density field formulation follows that of Manoharan³⁶ and are defined by

$$T_0(x, r) = T_C \left[\frac{1 + TR}{2} + \frac{1 - TR}{2} \tanh \left(\frac{r - r_f(x)}{\delta_f} \right) \right], \quad (A8)$$

$$\rho_0(x, r) = \rho_C \left[\frac{1 + DR}{2} + \frac{1 - DR}{2} \tanh \left(\frac{r - r_f(x)}{\delta_f} \right) \right]. \quad (A9)$$

δ_f controls the transition region width and models the preheat and reaction zone, and r_f is the reaction layer center location relative to the chamber center. r_f and d_f are derived from the mean OH* intensity distribution obtained from chemiluminescence imaging. Although chemiluminescence emissions imaging is a line-of-sight integrated technique, the mean reaction zone location can be readily identified from this measurement.

Figure 19(a) shows the top half of the mean image of a flame A based on 1000 frames, which is the result of a spatial average of the upper and lower half of the complete image. Figure 19(b) shows extracted radial intensity profiles from the image in Fig. 19(a) for which the axial extraction locations are color marked. For each axial location, a running average is computed based on a window length of 15 pixels in the r -direction. For each profile, a maximum is identified (dashed line), which, for a large enough sample, will closely correspond to the radial location of highest heat release and is thus assumed to be a fair approximation of the radial position of the temperature and density profile inflection point r_f .

The thickness of the T_0 and ρ_0 transition zone is approximated with the difference between the radial location of I_{max} and I_{99} , which is determined by the radial location for which the intensity profile decreased to $I(r) = 0.99I_{max}$. As the shear layer growth with axial distance from the sudden expansion and the potential mixture jet core area decreases, the local ratio of burned to unburned gas increases, leading to larger conductive heat transfer into the cold mixture jet core and thus to an increase in the preheat zone width. Both quantities are shown in Figs. 19(c) and 19(d), as well as the polynomials fitted to the samples. For the inflection point center r_f , a polynomial of degree 5 is used, whereas a linear curve fit is used for the transition half-width δ_f . The radial derivatives of the density and temperature fields are given as

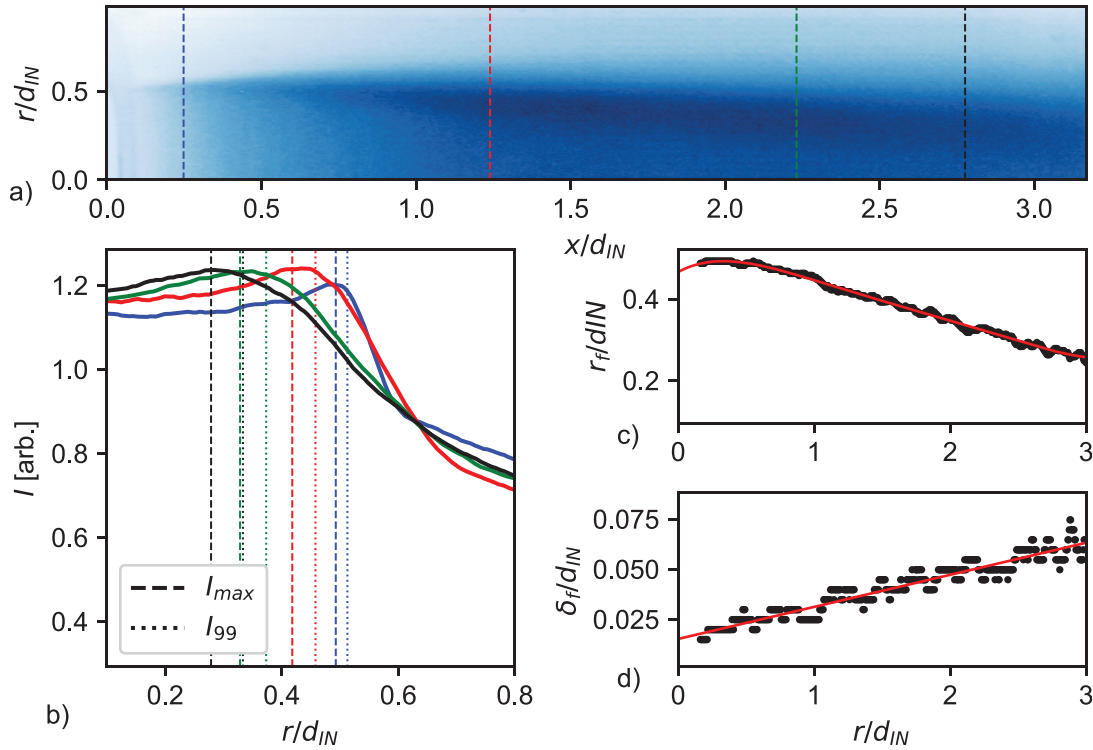


FIG. 19. (a) Mean OH* chemiluminescence intensity (top half) for flame A, (b) radial intensity profiles with marked positions of I_{max} and I_{99} , (c) radial location of I_{max} and polynomial curve fit representing r_f , (d) difference $r(I_{99}) - r(I_{max})$ and linear curve fit representing δ_f .

$$\frac{dT_0(x, r)}{dr} = T_{CH} \left[\frac{1 - TR}{2\delta_f} \cosh^{-2} \left(\frac{r - r_f(x)}{\delta_f(x)} \right) \right], \quad (A10)$$

$$\frac{d\rho_0(x, r)}{dr} = \rho_{CH} \left[\frac{1 - DR}{2\delta_f} \cosh^{-2} \left(\frac{r - r_f(x)}{\delta_f(x)} \right) \right], \quad (A11)$$

where $r_f(x)$ and $\delta_f(x)$ are locally defined by three respective polynomials.

The resulting base flow formulation is summarized in Fig. 20, which was generated using the operation conditions of flame B. Changes in flame length lead to different levels of interaction between the reaction and shear layer, as the temperature/density derivative location relative to the axial velocity derivative is altered.

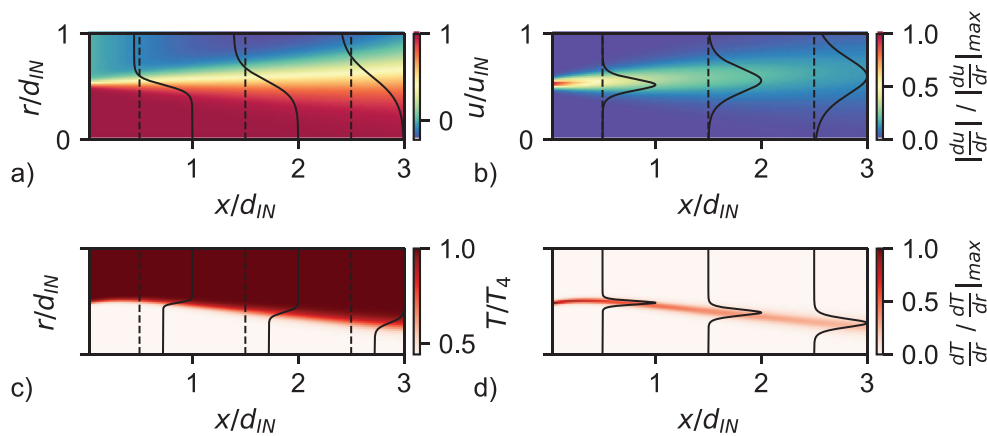


FIG. 20. Reconstructed base flow field for linear stability analysis: (a) axial velocity u_0 normalized by u_{IN} , (b) magnitude of axial velocity gradient $|du/dr|$ normalized by $|du/dr|_{max}$, (c) local temperature T normalized by T_C , and (d) temperature gradient dT/dr normalized by dT/dr_{max} . Superimposed profiles are normalized by their respective maximum.

Velocity, temperature, and density derivatives also vary drastically for the different operation conditions, leading to a complex interaction between the different instability source terms which will be shown to affect the shear layer stability and possible resonant modes inherent in the flow field.

APPENDIX B: RADIAL MODEL FORMULATION

A linear stability analysis of the base flow model formulated in Appendix A is performed assuming inviscid and locally parallel flow. At a specific axial location, the compressible Euler equations and energy equation in cylindrical coordinates x , r , and θ are linearized. Utilizing Reynolds decomposition, axial, radial, and azimuthal velocities u , v , and w and the gas state variables p , T , and ρ are decomposed as $q = q_0 + q'$, where q_0 and q' are the unperturbed base state and the superimposed perturbation, respectively. Rewriting the governing equations with decomposed variables and neglecting higher order terms and products of perturbation quantities, these equations reduce to

$$\frac{1}{\rho_0} \frac{\partial \rho'}{\partial t} + \frac{u_0}{\rho_0} \frac{\partial \rho'}{\partial x} + \frac{1}{r} \frac{\partial u'}{\partial x} + v' \left(\frac{1}{r} + \frac{1}{\rho_0} \frac{\partial \rho_0}{\partial r} \right) + \frac{\partial v'}{\partial r} + \frac{1}{r} \frac{\partial w'}{\partial \theta} = 0, \quad (\text{B1})$$

$$\frac{\partial u'}{\partial t} + u_0 \frac{\partial u'}{\partial x} + v' \frac{\partial u_0}{\partial r} = -\frac{1}{\rho_0} \frac{\partial p'}{\partial x}, \quad (\text{B2})$$

$$\frac{\partial v'}{\partial t} + u_0 \frac{\partial v'}{\partial x} = -\frac{1}{\rho_0} \frac{\partial p'}{\partial r}, \quad (\text{B3})$$

$$\frac{\partial w'}{\partial t} + u_0 \frac{\partial w'}{\partial x} = -\frac{1}{r \rho_0} \frac{\partial p'}{\partial \theta}, \quad (\text{B4})$$

$$c_p \rho_0 \left(\frac{\partial T'}{\partial t} + u_0 \frac{\partial T'}{\partial x} + v' \frac{\partial T_0}{\partial r} \right) = \frac{\partial p'}{\partial t} + u_0 \frac{\partial p'}{\partial x}, \quad (\text{B5})$$

representing conservation of mass, momentum, and energy, respectively. Using the linearized equation of state

$$p' = R_s (T_0 \rho' + \rho_0 T'). \quad (\text{B6})$$

ρ' is eliminated, and the mass conservation equation is rewritten as

$$\frac{1}{R_s T_0 \rho_0} \frac{\partial p'}{\partial t} - \frac{1}{T_0} \frac{\partial T'}{\partial t} + \frac{u_0}{R_s T_0 \rho_0} \frac{\partial p'}{\partial x} - \frac{u_0}{T_0} \frac{\partial T'}{\partial x} + \frac{1}{r} \frac{\partial u'}{\partial x} + v' \left(\frac{1}{r} + \frac{1}{\rho_0} \frac{\partial \rho_0}{\partial r} \right) + \frac{\partial v'}{\partial r} + \frac{1}{r} \frac{\partial w'}{\partial \theta} = 0, \quad (\text{B7})$$

reducing the system to the unknown perturbation variables $q' = [p', u', v', w', T']$, where R_s and c_p are the specific gas constant and the heat capacity at constant pressure. The gas medium in the domain is assumed to be air at a constant base flow pressure of p_{IN} with $R_s = 287 \text{ J/kgK}$. c_p is calculated for air at the given $T_0(r)$ using the thermophysical property library CoolProp.⁵¹ In order to investigate the stability characteristics of the flow field, a modal ansatz of the form

$$q'(x, r, \theta, t) = \hat{q}(r) e^{j(\alpha x + m\theta - \omega t)} \quad (\text{B8})$$

is employed, where $\hat{q} = [\hat{p}, \hat{u}, \hat{v}, \hat{w}, \hat{T}]^T$. The axial and temporal wave numbers $\alpha = \alpha_r + j\alpha_i$ and $\omega = \omega_r + j\omega_i$ are generally

complex, where the imaginary part describes the growth rate in space and time, respectively. ω_r is the angular frequency of the oscillation in time, whereas α_r defines the axial wavelength of the instability, where $\alpha_r = 2\pi/\lambda_x$ and λ_x is the physical wavelength in m. The azimuthal wave number m is an integer that describes the periodicity over the azimuthal coordinate θ and is positive or negative, describing instabilities traveling in opposed angular direction. Utilizing the ansatz in Eqs. (B2)–(B7) and casting the system into a discrete formulation yield

$$\frac{\alpha u_0}{\rho_0 R_s T_0} \hat{p} + \alpha \hat{u} - j \left(\frac{1}{r} + \frac{1}{\rho_0} \frac{d\rho_0}{dr} + \frac{d}{dr} \right) \hat{v} + \frac{m}{r} \hat{w} - \frac{\alpha u_0}{T_0} \hat{T} = \omega \left(\frac{1}{\rho_0 R_s T_0} \hat{p} - \frac{1}{T_0} \hat{T} \right), \quad (\text{B9})$$

$$\frac{\alpha u_0}{\rho_0} \hat{p} + \alpha u_0 \hat{u} - j \frac{du_0}{dr} \hat{v} = \omega \hat{u}, \quad (\text{B10})$$

$$-j \frac{d\hat{p}}{\rho_0 dr} + \alpha u_0 \hat{v} = \omega \hat{v}, \quad (\text{B11})$$

$$\frac{m}{r \rho_0} \hat{p} + \alpha u_0 \hat{w} = \omega \hat{w}, \quad (\text{B12})$$

$$-\alpha u_0 \hat{p} - j c_p \rho_0 \frac{dT_0}{dr} \hat{v} + \alpha c_p \rho_0 u_0 \hat{T} = \omega (-\hat{p} + c_p \rho_0 \hat{T}). \quad (\text{B13})$$

A generalized eigenvalue problem can now be formulated for the given system of equations as

$$\mathbf{A} \hat{\mathbf{q}} = \omega \mathbf{B} \hat{\mathbf{q}}. \quad (\text{B14})$$

Given that the flow field in this configuration is reasonably parallel compared to flow fields with a mean swirl component, a local LSA is justified. The aim for this analysis is to study the confined jet stability characteristics in the presence of an inhomogeneous density and temperature distribution and its spectral receptivity to perturbations within the range of the observed dynamics. The computational domain is bounded by the combustor wall at $r = r_{CC} = d_{IN}$, where the boundary condition $v'(r_{CC}) = 0$ is enforced. The domain is discretized with a staggered grid approach for which p' , u' , w' , and T' are evaluated at the center of $N = 250$ segments and the radial velocity perturbations v' at the $N + 1$ segment boundaries.

APPENDIX C: BASE FLOW RECONSTRUCTION FOR AXIAL MODEL

The base flow of the combustor for an axial acoustic analysis can be divided into three domains. The majority of the inlet flow field is homogeneous and comprised of the natural gas–air mixture at the inlet gas temperature T_{IN} . As the molecular weight of the mixture at the lean equivalence ratios of interest is similar to that of air, the fluid in the entire domain is assumed to be air with $R_s = 287 \text{ J/kgK}$. For the entire computational domain, a reference pressure of $p_0 = p_{IN}$ is assumed.

A second zone can be identified as the flame zone that contains the mixture jet potential core at T_{IN} , the recirculation zone comprised of reaction products at T_C , and the shear layer that is formed between the former. As the mixture is consumed, the cross-sectional area of the mixture jet decreases downstream of the sudden expansion, leading to an axially increasing mean temperature.

TABLE II. Estimated mean flame length for analyzed operating conditions.

Case	ϕ (...)	p_{IN} (bar)	T_{IN} (K)	T_{ad} (K)	u_{IN} (m/s)	l_f/d_{IN} (...)
Flame A	0.76	7.2	764	2280	134	4.46
Flame B	0.65	6.7	720	2070	134	6.14
Flame C	0.70	6.9	623	2073	115	6.41
Flame D	0.79	7.1	617	2217	110	5.44

This temperature profile can be estimated by evaluating the flame cross-sectional area. Assuming the flame is of a conical shape, the flame area reads

$$A_f(x) = \frac{\pi d_{IN}^2}{4} \left(1 - \frac{(x - l_{IN})^2}{l_f^2} \right), \quad (C1)$$

where $l_{IN} = 0.72$ m is the inlet length, $x = 0$ defines the domain inlet, and l_f is the mean flame length.

To estimate the mean flame length at a given operating condition, the laminar flame speed is computed using CANTERA,⁵² where a NG-air mixture defined by the global equivalence ratio ϕ is used and the gas state is defined by the inlet properties p_{IN} and T_{IN} . The turbulent flame speed S_t is then computed using the correlation presented by Ref. 53 using $u'_{rms} \approx 0.1 \cdot \bar{u}_{IN}$ and p_{IN} . A mean flame length for the four analyzed operating conditions is then estimated using a global reactant consumption speed formulation,⁵⁴ where $S_t = \dot{m}/(\bar{A}_f \rho_u)$. Table II lists the resulting flame lengths assuming a conical flame. The flame lengths derived from this analysis are only utilized for the axial base flow formulation.

The third sub-domain defines the remaining part of the combustion chamber for which the fluid field is homogeneous at the product temperature T_C . As direct gas temperature measurements in the combustion chamber were not obtained in the current experiment, two cases can be distinguished: either the combustion product temperature is estimated with the adiabatic flame temperature T_{ad} or a gas temperature is calculated, based on choked nozzle relations, measured chamber pressure and the total mass flow rate into the system.

Each gas state variable can be described by the gas temperature $T_0(x)$, which is given for the flame zone ($l_{IN} < x \leq l_{IN} + l_f$) as

$$T_0(x) = \frac{A_f(x)T_{IN} + (A_{CC} - A_f(x))T_C}{A_{CC}}, \quad (C2)$$

where $A_{CC} = \pi d_{CC}^2/4$ is the cross-sectional area of the combustion chamber with diameter $d_{CC} = 0.08$ m. The preheat zone length is estimated as $l_{preheat} = 0.05$ m, over which $T_0(x)$ is assumed to increase exponentially from T_{IN} to the temperature at the sudden expansion plane, given by $T_0(l_{IN})$. The temperature profile then reads for $l_{IN} - l_{preheat} < x \leq l_{IN}$,

$$T_0(x) = T_{IN} \exp \left[\log \left(\frac{T_0(l_{IN})}{T_{IN}} \right) \frac{x - (l_{IN} - l_{preheat})}{l_{preheat}} \right]. \quad (C3)$$

For $x \leq l_{IN} - l_{preheat}$ and $x > l_{IN} + l_f$, T_0 is given by T_{IN} and T_C , respectively.

Utilizing the ideal gas law, the axial density profile for $l_{IN} - l_{preheat} < x \leq l_{IN} + l_f$ is determined by

$$\rho_0(x) = \frac{p_0}{R_s T_0(x)}, \quad (C4)$$

whereas for $x \leq l_{IN} - l_{preheat}$ and $x > l_{IN} + l_f$, ρ_0 is given by ρ_{IN} and ρ_C , which are computed with CoolProp⁵¹ for air at gas states p_0 , T_{IN} and p_0 , T_C , respectively.

The conservation of the total mass flow \dot{m}_{tot} through the system then yields the axial velocity profile for $l_{IN} - l_{preheat} < x \leq l_{IN} + l_f$,

$$u_0(x) = \frac{\dot{m}_{tot}}{\rho_0(x)A}, \quad (C5)$$

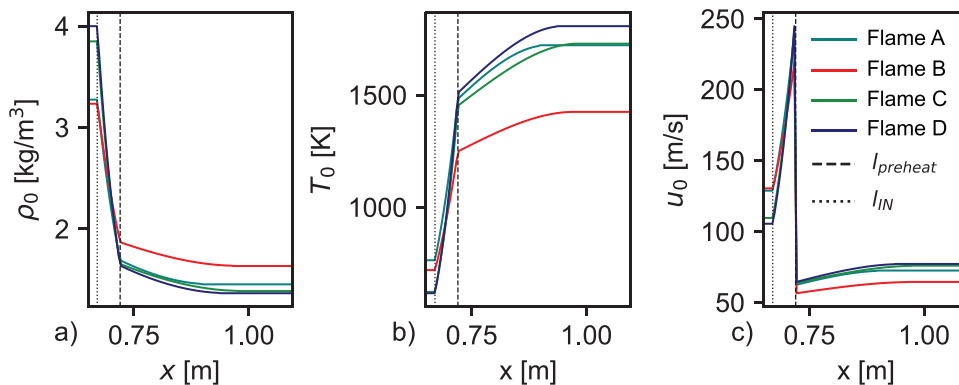
where A is the local cross-sectional area, A_{IN} for $x \leq l_{IN}$, and A_{CC} for $x > l_{IN}$.

The derivative of T_0 in the preheat zone $l_{IN} - l_{preheat} < x \leq l_{IN}$ is given by

$$\frac{dT_0(x)}{dx} = T_0(x) \log \left(\frac{T_0(l_{IN})}{T_3} \right) \frac{x - (l_{IN} - l_{preheat})}{l_{preheat}}, \quad (C6)$$

whereas in the flame zone for $l_{IN} < x \leq l_{IN} + l_f$ the profile is given as

$$\frac{dT_0(x)}{dx} = \frac{T_{IN} - T_C}{A_{CC}} \frac{dA_f(x)}{dx} \quad (C7)$$

**FIG. 21.** Axial model base flow profiles: (a) density ρ_0 , (b) temperature T_0 , and (c) mean axial velocity u_0 for each flame with marked preheat zone and dump plane location.

for all other x , $dT_0(x)/dx = 0$. The flame area derivative used here is defined as

$$\frac{dA_f(x)}{dx} = -\frac{\pi d_{IN}^2}{2l_f} \left(1 - \frac{x - l_{IN}}{l_f}\right). \quad (C8)$$

The velocity and density derivatives in the preheat and flame zone are then given by

$$\frac{du_0(x)}{dx} = \frac{\dot{m}_{tot} R_s}{p_0 A_{CC}} \frac{dT_0(x)}{dx}, \quad (C9)$$

$$\frac{\rho_0(x)}{dx} = -\frac{p_0}{R_s T_0^2(x)} \frac{dT_0(x)}{dx}, \quad (C10)$$

whereas in the remaining domain, these derivatives are zero. Figure 21 presents the resulting gas property profiles in the preheat and flame zone for each flame.

APPENDIX D: AXIAL MODEL FORMULATION

To analyze the systems longitudinal acoustic characteristics, a one-dimensional axial model of the combustor is formulated based on the inviscid compressible Euler equations. The linearized mass, axial momentum, and energy conservation equations with the axial coordinate x and velocity $u = u_0 + u'$ read

$$\frac{\partial \rho'}{\partial t} + \rho_0 \frac{\partial u'}{\partial x} + u_0 \frac{\partial \rho'}{\partial x} + \rho' \frac{\partial u_0}{\partial x} + u' \frac{\partial \rho_0}{\partial x} = 0, \quad (D1)$$

$$\rho_0 \left(\frac{\partial u'}{\partial t} + u_0 \frac{\partial u'}{\partial x} + u' \frac{\partial u_0}{\partial x} \right) + u_0 \frac{\partial \rho_0}{\partial x} \rho' = -\frac{\partial p'}{\partial x}, \quad (D2)$$

$$c_p \rho_0 \left(\frac{\partial T'}{\partial t} + u_0 \frac{\partial T'}{\partial x} + u' \frac{\partial T_0}{\partial x} \right) + c_p u_0 \frac{\partial T_0}{\partial x} \rho' = \frac{\partial p'}{\partial t} + u_0 \frac{\partial p'}{\partial x}. \quad (D3)$$

Substituting the linearized equation of state $p' = R_s(T_0 \rho' + T' \rho_0)$ to eliminate ρ' from the system of equation and rearranging gives the governing equations with the unknown perturbation variables $q' = [p', u', T']^T$,

$$\begin{aligned} & \left(\frac{1}{R_s T_0} \frac{\partial u_0}{\partial x} - \frac{u_0}{R_s T_0^2} \frac{\partial T_0}{\partial x} \right) p' + \frac{u_0}{R_s T_0} \frac{\partial p'}{\partial x} + \frac{\partial \rho_0}{\partial x} u' + \rho_0 \frac{\partial u'}{\partial x} \\ & + \left(\frac{u_0 \rho_0}{T_0^2} \frac{\partial T_0}{\partial x} - \frac{u_0}{T_0} \frac{\partial \rho_0}{\partial x} - \frac{\rho_0}{T_0} \frac{\partial u_0}{\partial x} \right) T' - \frac{u_0 \rho_0}{T_0} \frac{\partial T'}{\partial x} \\ & = -\frac{1}{R_s T_0} \frac{\partial p'}{\partial t} + \frac{\rho_0}{T_0} \frac{\partial T'}{\partial t}, \end{aligned} \quad (D4)$$

$$\frac{u_0}{R_s T_0} \frac{\partial u_0}{\partial x} p' + \frac{\partial p'}{\partial x} + \rho_0 \frac{\partial u_0}{\partial x} u' + \rho_0 u_0 \frac{\partial u'}{\partial x} - \frac{\rho_0 u_0}{T_0} \frac{\partial u_0}{\partial x} T' = -\rho_0 \frac{\partial u'}{\partial t}, \quad (D5)$$

$$\begin{aligned} & \frac{c_p u_0}{R_s T_0} \frac{\partial T_0}{\partial x} p' - u_0 \frac{\partial p'}{\partial x} + c_p \rho_0 \frac{\partial T_0}{\partial x} u' - \frac{c_p \rho_0 u_0}{T_0} \frac{\partial T_0}{\partial x} T' \\ & + c_p \rho_0 u_0 \frac{\partial T'}{\partial x} = \frac{\partial p'}{\partial t} - c_p \rho_0 \frac{\partial T'}{\partial t}. \end{aligned} \quad (D6)$$

In order to analyze the acoustic characteristics of the combustor, a modal ansatz of the form

$$q'(x, t) = \hat{q}(x) e^{-j\omega t} \quad (D7)$$

is employed, where $\hat{q} = [\hat{p}, \hat{u}, \hat{T}]^T$ and $\omega = \omega + j\omega_i$ are the temporal wave numbers. Utilizing this ansatz in Eqs. (D4) and (D5) and casting the system into a discrete formulation yield

$$\begin{aligned} & -j \left[\left(\frac{1}{R_s T_0} \frac{du_0}{dx} - \frac{u_0}{R_s T_0^2} \frac{dT_0}{dx} \right) \hat{p} + \frac{u_0}{R_s T_0} \frac{d\hat{p}}{dx} + \frac{d\rho_0}{dx} \hat{u} + \rho_0 \frac{d\hat{u}}{dx} \right. \\ & \left. + \left(\frac{u_0 \rho_0}{T_0^2} \frac{dT_0}{dx} - \frac{u_0}{T_0} \frac{d\rho_0}{dx} - \frac{\rho_0}{T_0} \frac{du_0}{dx} \right) \hat{T} - \frac{u_0 \rho_0}{T_0} \frac{d\hat{T}}{dx} \right] \\ & = \omega \left(\frac{1}{R_s T_0} \frac{d\hat{p}}{dx} - \frac{\rho_0}{T_0} \frac{d\hat{T}}{dx} \right), \end{aligned} \quad (D8)$$

$$-j \left(\frac{u_0}{R_s T_0} \frac{du_0}{dx} \hat{p} + \frac{d\hat{p}}{dx} + \rho_0 \frac{du_0}{dx} \hat{u} + \rho_0 u_0 \frac{d\hat{u}}{dx} - \frac{\rho_0 u_0}{T_0} \frac{du_0}{dx} \hat{T} \right) = \omega \rho_0 \hat{u}, \quad (D9)$$

$$\begin{aligned} & -j \left(\frac{c_p u_0}{R_s T_0} \frac{dT_0}{dx} \hat{p} - u_0 \frac{d\hat{p}}{dx} + c_p \rho_0 \frac{dT_0}{dx} \hat{u} - \frac{c_p \rho_0 u_0}{T_0} \frac{dT_0}{dx} \hat{T} + c_p \rho_0 u_0 \frac{d\hat{T}}{dx} \right) \\ & = \omega \left(-\hat{p} + c_p \rho_0 \hat{T} \right). \end{aligned} \quad (D10)$$

A generalized eigenvalue problem is formulated for the given system of equations as

$$A \hat{q} = \omega B \hat{q}. \quad (D11)$$

The discretized combustor model is comprised of two domains: the inlet and the combustion chamber with the cross-sectional areas A_{IN} and A_{CC} and lengths l_{IN} and l_{CC} , respectively. The computational domain is bounded by the combustor inlet at $x=0$ and outlet $x=l_{IN}+l_{CC}=1.92$ m, where the boundary condition $u'=0$ is enforced that reflects the flow conditions at the throat of the sonic nozzles. Each sub-domain is discretized with a staggered grid approach for which p' and T' are evaluated at the center of $N=150$ segments and the axial velocity perturbations u' at the $N+1$ segment boundaries.

At the interface of the two domains, the area change is incorporated by employing velocity and pressure relations that follow the numerical approach of Lin *et al.*⁵⁵ and Migliorino and Scalo⁵⁶

$$-\hat{p}_{IN}[N-1] + 3\hat{p}_{IN}[N] = 3\hat{p}_{CC}[1] - \hat{p}_{CC}[2], \quad (D12)$$

$$\hat{u}_{IN}[N+1]\rho(l_{IN})A_{IN} = \hat{u}_{CC}[1]\rho(l_{IN})A_{CC}. \quad (D13)$$

Thus, at the plane of sudden expansion, the pressure and mass flow rate fluctuations are set equal between the two domains.

Figure 22 presents the eigenspectrum of the combustor longitudinal acoustics for flame A with $T_C=1722$ K, corresponding to the mean gas temperature in the chamber. This temperature is computed from the measured static chamber pressure and known mass flow rate through the sonic exit nozzle. The fundamental longitudinal modes are located close to the real axis of the spectrum in Fig. 22(a). The spectrum is symmetric about the imaginary axis, representing the forward and backward running waves in the system. Additional branches are identified, which correspond to modes that are dominant in the inlet, flame zone [red shaded area in Figs. 22(b) and 22(c)] or combustion chamber. The eigenvectors for

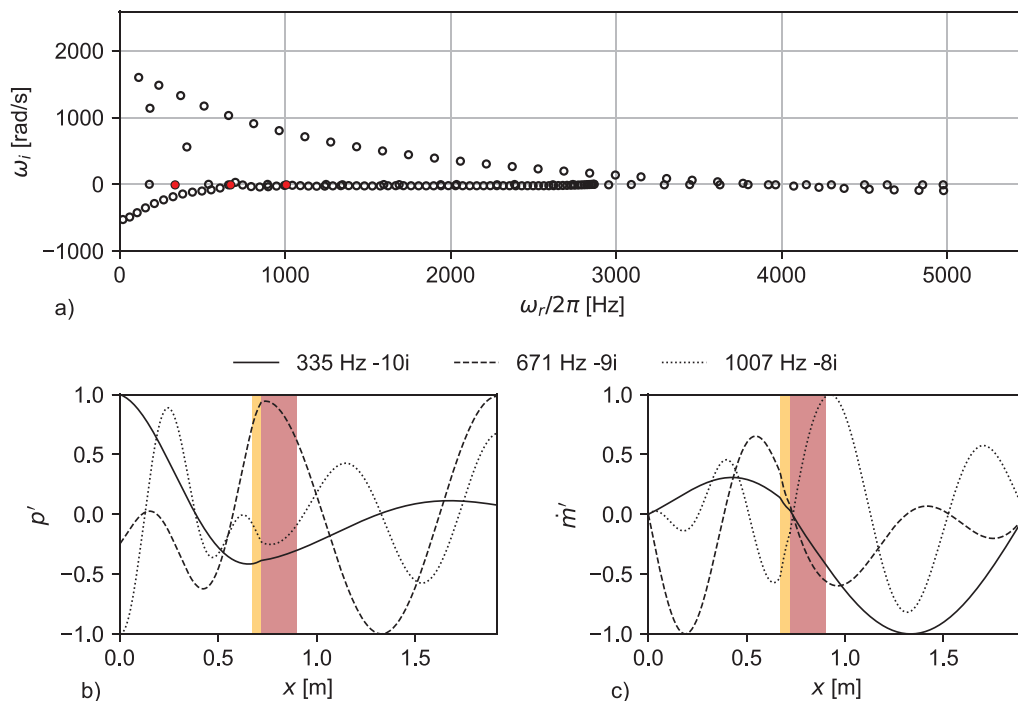


FIG. 22. (a) Eigenvalue spectrum of axial model solutions (only right-hand side of spectrum is shown): (filled red circles) 1L, 2L, and 3L modes. (b) and (c) p' and \dot{m}' eigenvec-tors of 1L, 2L, and 3L modes, respectively.

p' and $\dot{m}' = \rho Au'$ representing the 1L, 2L, and 3L modes are shown in Figs. 2(a) and 2(b). The flame zone is observed to have an increasing influence on the mode shape with decreasing axial wave-length, indicating the increased spatial correlation between temper-ature gradients and acoustic field in the combustor.

REFERENCES

- ¹B. T. Zinn and T. C. Lieuwen, "Combustion instabilities: Basic concepts," *Combust. Instab. Gas Turbine Eng.* **210**, 3–26 (2005).
- ²S. Ducruix, T. Schuller, D. Durox, and S. Candel, "Combustion instability mechanisms in premixed combustors," *Prog. Astronaut. Aeronaut.* **210**, 179 (2005).
- ³A. P. Dowling and A. S. Morgans, "Feedback control of combustion oscillations," *Annu. Rev. Fluid Mech.* **37**, 151–182 (2005).
- ⁴J. O'Connor, V. Acharya, and T. Lieuwen, "Transverse combustion instabilities: Acoustic, fluid mechanic, and flame processes," *Prog. Energy Combust. Sci.* **49**, 1–39 (2015).
- ⁵T. Schuller, T. Poinso, and S. Candel, "Dynamics and control of premixed combustion systems based on flame transfer and describing functions," *J. Fluid Mech.* **894**, P1 (2020).
- ⁶P. Kasthuri, S. A. Pawar, R. Gejji, W. Anderson, and R. I. Sujith, "Coupled interaction between acoustics and unsteady flame dynamics during the transition to thermoacoustic instability in a multi-element rocket combustor," *Combust. Flame* **240**, 112047 (2022).
- ⁷P. Kasthuri, A. Krishnan, R. Gejji, W. Anderson, N. Marwan, J. Kurths, and R. I. Sujith, "Investigation into the coherence of flame intensity oscillations in a model multi-element rocket combustor using complex networks," *Phys. Fluids* **34**, 034107 (2022).
- ⁸T. Poinso, "Prediction and control of combustion instabilities in real engines," *Proc. Combust. Inst.* **36**, 1–28 (2017).
- ⁹J. S. Hardi, S. K. Beinke, M. Oswald, and B. B. Dally, "Coupling of cryogenic oxygen–hydrogen flames to longitudinal and transverse acoustic instabilities," *J. Propul. Power* **30**, 991–1004 (2014).
- ¹⁰A. Urbano, L. Selle, G. Staffelbach, B. Cuenot, T. Schmitt, S. Ducruix, and S. Candel, "Exploration of combustion instability triggering using large eddy simulation of a multiple injector liquid rocket engine," *Combust. Flame* **169**, 129–140 (2016).
- ¹¹M. Sliphorst, S. Gröning, and M. Oswald, "Theoretical and experimental identification of acoustic spinning mode in a cylindrical combustor," *J. Propul. Power* **27**, 182–189 (2011).
- ¹²T. Hummel, F. Berger, M. Hertweck, B. Schuermans, and T. Sattelmayer, "High-frequency thermoacoustic modulation mechanisms in swirl-stabilized gas turbine combustors—Part II: Modeling and analysis," *J. Eng. Gas Turbines Power* **139**, 071502 (2017).
- ¹³F. M. Berger, T. Hummel, M. Hertweck, J. Kaufmann, B. Schuermans, and T. Sattelmayer, "High-frequency thermoacoustic modulation mechanisms in swirl-stabilized gas turbine combustors—Part I: Experimental investigation of local flame response," *J. Eng. Gas Turbines Power* **139**, 071501 (2017).
- ¹⁴T. Buschhagen, R. Gejji, J. Philo, L. Tran, J. E. P. Bilbao, and C. D. Slabaugh, "Self-excited transverse combustion instabilities in a high pressure lean pre-mixed jet flame," *Proc. Combust. Inst.* **37**, 5181 (2019).
- ¹⁵N. A. Worth, D. Mistry, T. Berk, and J. R. Dawson, "Vortex dynamics of a jet at the pressure node in a standing wave," *J. Fluid Mech.* **882**, A22 (2020).
- ¹⁶N. A. Worth and J. R. Dawson, "Modal dynamics of self-excited azimuthal instabilities in an annular combustion chamber," *Combust. Flame* **160**, 2476–2489 (2013).
- ¹⁷J. J. Philo, R. M. Gejji, and C. D. Slabaugh, "Injector-coupled transverse instabilities in a multi-element premixed combustor," *Int. J. Spray Combust. Dyn.* **12**, 175682772093283 (2020).
- ¹⁸T. C. Lieuwen, "Hydrodynamic flow stability I: Introduction," in *Unsteady Combustor Physics* (Cambridge University Press, 2012), pp. 50–71.
- ¹⁹T. C. Lieuwen, "Hydrodynamic flow stability II: Common combustor flow fields," in *Unsteady Combustor Physics* (Cambridge University Press, 2012), pp. 72–123.
- ²⁰D. A. Smith and E. E. Zukoski, "Combustion instability sustained by unsteady vortex combustion," in *21st Joint Propulsion Conference* (AIAA, 1985), p. 1248.

- ²¹T. J. Poinso, A. C. Trounev, D. P. Veynante, S. M. Candel, and E. J. Esposito, "Vortex-driven acoustically coupled combustion instabilities," *J. Fluid Mech.* **177**, 265–292 (1987).
- ²²K. Venkataraman, L. Preston, D. Simons, B. Lee, J. Lee, and D. Santavicca, "Mechanism of combustion instability in a lean premixed dump combustor," *J. Propul. Power* **15**, 909–918 (1999).
- ²³M. Stöhr, R. Sadanandan, and W. Meier, "Experimental study of unsteady flame structures of an oscillating swirl flame in a gas turbine model combustor," *Proc. Combust. Inst.* **32**, 2925–2932 (2009).
- ²⁴R. Sampath and S. R. Chakravarthy, "Investigation of intermittent oscillations in a premixed dump combustor using time-resolved particle image velocimetry," *Combust. Flame* **172**, 309–325 (2016).
- ²⁵S. Hong, R. L. Speth, S. J. Shanbhogue, and A. F. Ghoniem, "Examining flow–flame interaction and the characteristic stretch rate in vortex-driven combustion dynamics using PIV and numerical simulation," *Combust. Flame* **160**, 1381–1397 (2013).
- ²⁶D. E. Rogers and F. E. Marble, "A mechanism for high frequency oscillations in ramjet combustors and afterburners," *Jet Propul.* **26**, 456–462 (1956).
- ²⁷M. P. Juniper, "The full impulse response of two-dimensional jet/wake flows and implications for confinement," *J. Fluid Mech.* **590**, 163–185 (2007).
- ²⁸M. P. Juniper, "The effect of confinement on the stability of non-swirling round jet/wake flows," *J. Fluid Mech.* **605**, 227–252 (2008).
- ²⁹E. Æsøy, J. G. Aguilar, N. A. Worth, and J. R. Dawson, "The response of an axisymmetric jet placed at various positions in a standing wave," *J. Fluid Mech.* **917**, A16 (2021).
- ³⁰I. Danaïla and B. J. Boersma, "Direct numerical simulation of bifurcating jets," *Phys. Fluids* **12**, 1255–1257 (2000).
- ³¹P. Huerre and P. A. Monkewitz, "Absolute and convective instabilities in free shear layers," *J. Fluid Mech.* **159**, 151–168 (1985).
- ³²P. Huerre and P. A. Monkewitz, "Local and global instabilities in spatially developing flows," *Annu. Rev. Fluid Mech.* **22**, 473–537 (1990).
- ³³M. P. Juniper and S. M. Candel, "The stability of ducted compound flows and consequences for the geometry of coaxial injectors," *J. Fluid Mech.* **482**, 257–269 (2003).
- ³⁴A. F. Ghoniem, A. Annaswamy, D. Wee, T. Yi, and S. Park, "Shear flow-driven combustion instability: Evidence, simulation, and modeling," *Proc. Combust. Inst.* **29**, 53–60 (2002).
- ³⁵M. P. Juniper, "Absolute and convective instability in gas turbine fuel injectors," in *ASME Turbo Expo 2012: Turbine Technical Conference and Exposition* (American Society of Mechanical Engineers, 2012), pp. 189–198.
- ³⁶K. Manoharan and S. Hemchandra, "Absolute/convective instability transition in a backward facing step combustor: Fundamental mechanism and influence of density gradient," *J. Eng. Gas Turbines Power* **137**, 021501 (2015).
- ³⁷K. Oberleithner, M. Stöhr, S. H. Im, C. M. Arndt, and A. M. Steinberg, "Formation and flame-induced suppression of the precessing vortex core in a swirl combustor: Experiments and linear stability analysis," *Combust. Flame* **162**, 3100–3114 (2015).
- ³⁸P. Paredes, S. Terhaar, K. Oberleithner, V. Theofilis, and C. Oliver Paschereit, "Global and local hydrodynamic stability analysis as a tool for combustor dynamics modeling," *J. Eng. Gas Turbines Power* **138**, 021504 (2016).
- ³⁹T. Buschhagen, R. Gejji, J. Philo, L. Tran, J. E. P. Bilbao, and C. D. Slabaugh, "Experimental investigation of self-excited combustion instabilities in a lean, premixed, gas turbine combustor at high pressure," *J. Eng. Gas Turbines Power* **140**, 111503 (2018).
- ⁴⁰R. M. Gejji, T. Buschhagen, and C. D. Slabaugh, "Occurrence of rotating detonation waves in a jet-stabilized combustor with premixed injection," *J. Propul. Power* **37**, 645–645 (2021).
- ⁴¹American Society of Mechanical Engineers, *Measurement of Gas Flow by Means of Critical Flow Venturis and Critical Flow Nozzles* (American Society of Mechanical Engineers, 2016).
- ⁴²International Standards Organization, *Measurement of Gas Flow by Means of Critical Flow Venturi Nozzles* (International Standards Organization, 2005).
- ⁴³C. D. Slabaugh, A. C. Pratt, R. P. Lucht, S. E. Meyer, M. Benjamin, K. Lyle, and M. Kelsey, "The development of an optically accessible, high-power combustion test rig," *Rev. Sci. Instrum.* **85**, 035105 (2014).
- ⁴⁴C. A. Fugger, R. M. Gejji, J. E. Portillo, Y. Yu, R. P. Lucht, and W. E. Anderson, "A model combustor for studying a reacting jet in an oscillating crossflow," *Rev. Sci. Instrum.* **88**, 065112 (2017).
- ⁴⁵R. M. Gejji, I. V. Walters, S. Beard, A. Lemcherfi, S. V. Sardeshmukh, S. D. Heister, and C. D. Slabaugh, "Transducer installation effects on pressure measurements in PGC devices," AIAA Paper No. 2018-0158, 2018.
- ⁴⁶A. Towne, O. T. Schmidt, and T. Colonius, "Spectral proper orthogonal decomposition and its relationship to dynamic mode decomposition and resolvent analysis," *J. Fluid Mech.* **847**, 821–867 (2018).
- ⁴⁷A. Michalke, "Survey on jet instability theory," *Prog. Aerosp. Sci.* **21**, 159–199 (1984).
- ⁴⁸S. B. Pope, *Turbulent Flows* (Cambridge University Press, 2000).
- ⁴⁹W. H. Stevenson, H. D. Thompson, and R. Gould, "Laser velocimeter measurements and analysis in turbulent flows with combustion. Part 2," Technical Report No. AFWAL-TR-82-2076, Purdue University Lafayette in School of Mechanical Engineering, 1983.
- ⁵⁰R. W. Pitz and J. W. Daily, "Combustion in a turbulent mixing layer formed at a rearward-facing step," *AIAA J.* **21**, 1565–1570 (1983).
- ⁵¹I. H. Bell, J. Wronski, S. Quoilin, and V. Lemort, "Pure and pseudo-pure fluid thermophysical property evaluation and the open-source thermo-physical property library coolprop," *Ind. Eng. Chem. Res.* **53**, 2498–2508 (2014).
- ⁵²D. G. Goodwin, R. L. Speth, H. K. Moffat, and B. W. Weber, "Cantera: An object-oriented software toolkit for chemical kinetics, thermodynamics, and transport processes," Version 2.4.0 (2018).
- ⁵³H. Kobayashi, "Experimental study of high-pressure turbulent premixed flames," *Exp. Therm. Fluid Sci.* **26**, 375–387 (2002).
- ⁵⁴J. F. Driscoll, "Turbulent premixed combustion: Flamelet structure and its effect on turbulent burning velocities," *Prog. Energy Combust. Sci.* **34**, 91–134 (2008).
- ⁵⁵J. Lin, C. Scalò, and L. Hesselink, "High-fidelity simulation of a standing-wave thermoacoustic–piezoelectric engine," *J. Fluid Mech.* **808**, 19–60 (2016).
- ⁵⁶M. T. Migliorino and C. Scalò, "Real-fluid effects on standing-wave thermoacoustic instability," *J. Fluid Mech.* **883**, A23 (2020).